Ore Geology Reviews 105 (2019) 201–215

Contents lists available at ScienceDirect

Ore Geology Reviews

journal homepage: www.elsevier.com/locate/oregeorev

Multiple mineralization events in the Zhaxikang Sb–Pb–Zn–Ag deposit and their relationship with the geodynamic evolution in the North Himalayan Metallogenic Belt, South Tibet

Da Wang[a], Youye Zheng[a,b,*], Ryan Mathur[c], Junsheng Jiang[b], Sukun Zhang[d], Jianfang Zhang[e], Miao Yu[f]

[a] State Key Laboratory of Geological Processes and Mineral Resources, School of Earth Sciences and Resources, China University of Geosciences, Beijing 100083, China
[b] State Key Laboratory of Geological Processes and Mineral Resources, and Faculty of Earth Resources, China University of Geosciences, Wuhan 430074, China
[c] Department of Geology, Juniata College, Huntingdon, PA 16652, USA
[d] First Institute of Geological and Mineral Resources Survey, Hennan Geological Exploration Bureau, Luoyang 471023, China
[e] Zhejiang Institute of Geological Survey, Hangzhou 311203, China
[f] Beijing Institute of Geology, Beijing 100120, China

ARTICLE INFO

Keywords:
Zhaxikang deposit
Isotope geochronology
Three pulses of mineralization
Ore-forming model

ABSTRACT

The Zhaxikang Sb–Pb–Zn–Ag deposit, the only super-large deposit identified within the North Himalayan Metallogenic Belt (NHMB), is still debated to date with perspectives of mineralization age and genesis. The previous genetic models mainly include hot-spring, magmatic hydrothermal fluid, coarse-grained hydrothermal Pb–Zn vein overprinted by Sb-rich magmatic hydrothermal fluid, and SEDEX overprinted by hydrothermal fluid. Here, we present new and credible isotope geochronological evidence to discuss the genesis and mineralization age of Zhaxikang deposit. The isotopic ages of minerals from different mineralization stages in Zhaxikang deposit coincide with the mineralization ages of three main regional mineralization events. In detail, the older 206Pb/238U (218 ± 10 Ma), Sm–Nd (173.7 ± 7.4 Ma) and Rb–Sr (147 ± 3.2 Ma) isochron ages match three regional extensive seafloor volcanic events during synsedimentary period (220–130 Ma); the younger 206Pb/238U (62 ± 8.2 Ma) and older Re–Os (47.7 ± 7.9 Ma; 43.1 ± 2.5 Ma) ages are in accord with the formation age of regional orogenic Au–Sb deposits associated with metamorphic fluid system during syn-collision period (60–42 Ma); and the Ar–Ar (19.3 ± 1.1 Ma) and younger Re–Os (9.0 ± 1.9 Ma) isochron ages are consistent with the regional magmatic-hydrothermal mineralization event during post-collision period (25 Ma to now). We thus proposed that Zhaxikang deposit is a superimposed deposit that experienced three pulses of mineralization corresponding to three regional mineralization events: the first pulse of mineralization (stages 1 and 2) is related to multiple seafloor volcanic events during synsedimentary period with submarine hydrothermal sedimentation (metasomatism) genesis; the second pulse of mineralization (stages 3 and 4) is associated with metamorphic fluid system during syn-collision period that overprint the Pb–Zn mineralization; and the third pulse of mineralization (stages 5 and 6) relates to magmatic-hydrothermal activity during post-collision period and also overprints early mineralization. Furthermore, the complicated superimposed mineralization results in the discordance of different geochronological methods.

1. Introduction

The North Himalayan Metallogenic Belt (NHMB) is the important component of the Tethys-Himalaya Metallogenic Domain (Fig. 1A and B). Three main regional mineralization events have generated a series of Sb, Sb–Au, Au, Pb–Zn(Ag) and Sb–Pb–Zn–Ag deposits within NHMB, such as the Zhaxikang Sb–Pb–Zn–Ag, the Mazhala Au–Sb, the Chalapu Au, the Shalagang Sb deposits and so on (Fig. 1C; Yang et al., 2009; Zheng et al., 2012, 2014; Li et al., 2017). Detailedly, the first regional mineralization event is related to multiple seafloor volcanic events during synsedimentary period (220–130 Ma); the second regional mineralization event is associated with the metamorphic fluid system

* Corresponding author at: State Key Laboratory of Geological Processes and Mineral Resources, School of Earth Sciences and Resources, China University of Geosciences, Beijing 100083, China.
E-mail address: zhyouye@163.com (Y. Zheng).

https://doi.org/10.1016/j.oregeorev.2018.12.024
Received 3 April 2018; Received in revised form 13 December 2018; Accepted 28 December 2018
Available online 28 December 2018
0169-1368/

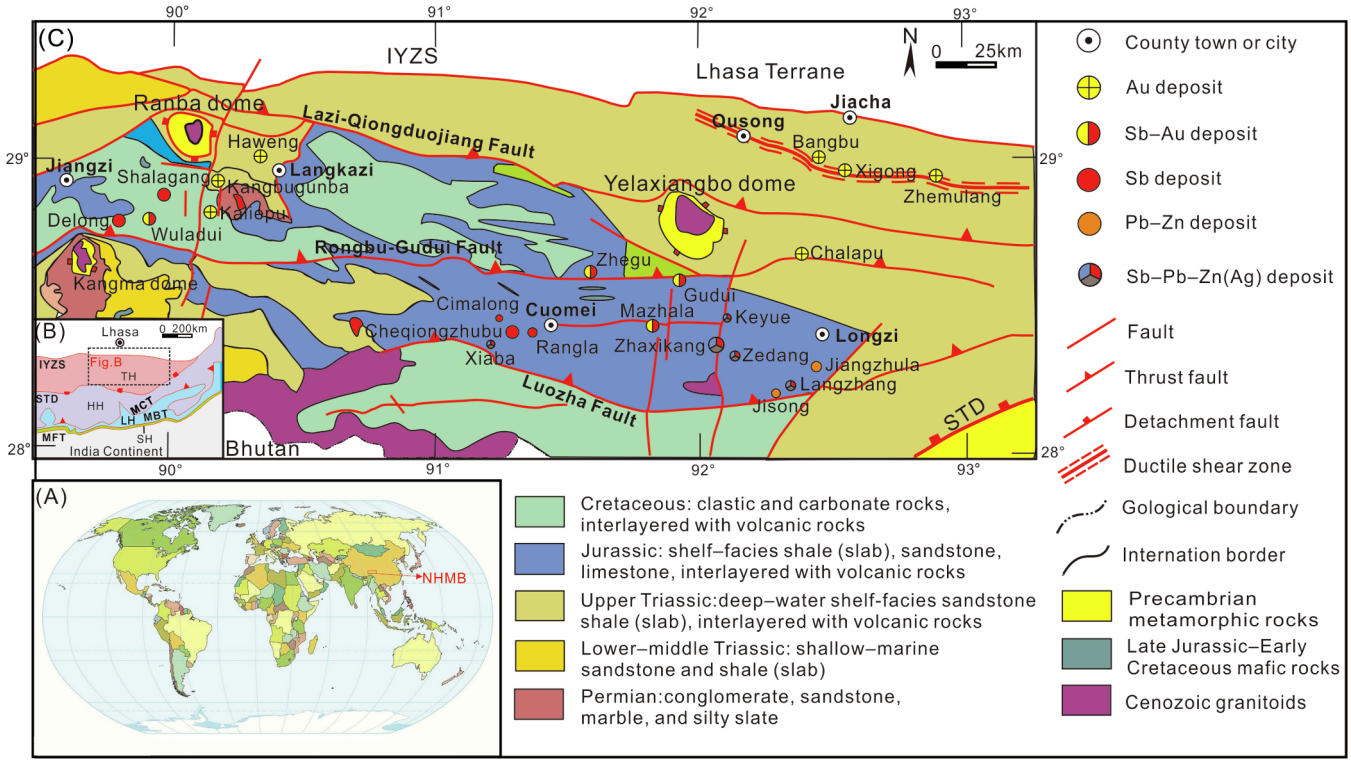

Fig. 1. (A) The global location of the NHMB. (B) Tectonic framework of the Himalayan Terrane (modified from Yin, 2006; Wang et al., 2018a). (C) Regional geological map of the North Himalayan Metallogenic Belt (modified from Zheng et al., 2014; Wang et al., 2018a). IYZS: the Indus-Yarlung Zangbo Suture Zone; STDS: the South Tibet Detachment System; MCT: the Main Central Thrust Fault; MBT: the Main Boundary Thrust Fault; MFT: the Main Frontal Thrust; NH: the North Himalayan Tethys sedimentary fold belt; HH: the High Himalayan crystalline rock belt; LH: the Low Himalayan fold belt; SH: the Sub-Himalayan tectonic belt.

during syn-collision period (60–42 Ma) that generated several orogenic Au–Sb deposits (e.g., Nianzha and Bangbu Au deposits); and the third regional mineralization event relates to the magmatic-hydrothermal activity during post-collision period (25 Ma to now) that formed some W–Sn, Pb–Zn(Ag) and Sb–Au deposits (e.g., Dongga W–Sn and Shalagang Sb deposits; Zheng et al., 2014; Li et al., 2017). The NHMB is an area with great interest to international community due to its complex tectonic and metallogenic history.

As the only super-large deposit within NHMB (Zn + Pb 2.066 Mt, grade 6.38%; Sb 0.235 Mt, grade 1.14%; Ag 2660.6 t, grade 101.64 g/t; Au 6.5 t, grade 2.9 g/t (independent gold ore body); associated Au 3.9 t and Ga 361 t; and 20 Mt Mn–Fe carbonates ores, Fe + Mn grade 42%), Zhaxikang deposit have been extensively studied (e.g., Wang et al., 2017; Sun et al., 2018). However, due to superposition of multiple generation hydrothermal events and lack of suitable dating methods, the genesis and mineralization age are still controversial. The previous genetic models are as follow: Meng et al. (2008) only paid attention to the Sb mineralization and constrained the hot spring genesis using Si–H–O isotopes. Similarly, according to S–Pb, H–O, He–Ar isotopic evidence, Zhang et al. (2010) thought that the hot spring circulation drived by tectonism leached ore-forming elements in wall-rocks and then filled along the faults to form Zhaxikang deposits. Based on Zn–S–Pb isotopes, Duan et al. (2016) regarded Zhaxikang deposit as a magmatic hydrothermal deposit with the ore-forming material sourcing from basement and sedimentary rocks. Analogously, the C–O isotopes and melt inclusions research from Xie et al. (2017) also supported the magmatic hydrothermal fluid genesis, yet Xie et al. (2017) considered the magmatic hydrothermal fluid is derived from differential evolution of immiscible magma. In addition, Zhou et al. (2018) measured Re–Os isochron age (43.1 ± 2.5 Ma; Table 1) and S–Pb isotopes of minerals and rocks from Zhaxikang deposit, and then proposed that Zhaxikang deposit is an epigenetic magmatic hydrothermal deposit rather than a syngenetic deposit. By comparison, other researchers deem Zhaxikang deposit to be a superimposed deposit. Through careful study of regional and deposit geology, elemental and fluid inclusion, Liang et al. (2013) suggested that the genetic model is coarse-grained hydrothermal Pb–Zn vein overprinted by Sb-rich magmatic hydrothermal fluid. However, Zheng et al. (2012) argued that the ore texture, geochronological, elemental and isotopic analyses are in favor of the SEDEX overprinted by hydrothermal fluid genetic model, which is also evidenced by the Fe–Zn isotopic evidence of Wang et al. (2018a).

The isotope geochronology research is beneficial to clarify ore-forming processes and ore genesis. Here, we present the Rb–Sr isochron age of stage 2 sphalerite, Sm–Nd isochron age of stages 1 and 2 Mn–Fe carbonate, Re–Os ages of stages 1 and 2 pyrite and $^{206}Pb/^{238}U$ ages of zircons from stages 1 and 2 Mn–Fe carbonate, combing with previous Ar–Ar isochron age of sericite in stage 5 quartz-pyrite-stibnite vein (Sun et al., 2018), to provide new and credible evidence for mineralization age and genesis of Zhaxikang deposit.

2. Geological setting

2.1. Regional geology

As important tectonic unit of the Cenozoic Himalayan-Tibetan orogen, the Himalayan Terrane is located between the Lhasa Terrane and India Continent and is divided into the North Himalayan Tectonic Belt (NH), the High Himalayan Crystalline Rock Belt (HH), the Low Himalayan Fold Belt (LH), and the Sub-Himalayan Tectonic Belt (SH), respectively (Fig. 1B; Harrison et al., 1992; Jeffrey et al., 2000; Yin and Harrison, 2000). These four tectonic belts are separated by four nearly EW-trending faults from north to south with the name of the South Tibet Detachment System (STDS), the Main Central Thrust (MCT), the Main Boundary Thrust (MBT) and the Main Frontal Thrust (MFT; Fig. 1B; Yin, 2000, 2006). The NHMB is in the eastern section of NH that records the sedimentary sequence including the Late Precambrian to Devonian pre-rift, Carboniferous to Early Jurassic syn-rift, and Middle Jurassic to Cretaceous passive continental margin sediments.

Table 1
The geochronological data of Zhaxikang deposit.

Analytical Method	Mineral/Rocks	Ages	Reference
Zircon SHRIMP U–Pb	Diabase	133 Ma	Zheng et al. (2012)
Zircon SHRIMP U–Pb	Rhyolite porphyry	135 Ma	Lin et al. (2014)
Ar–Ar	Sericite	19.3 ± 1.1 Ma	Sun et al. (2018)
Re–Os	Pyrite	43.1 ± 2.5 Ma	Zhou et al. (2018)
ESR	Quartz	18.3 ± 1.8 Ma, 20.3 ± 2.3 Ma	Zhang. (2010)
Zircon U–Pb	Mn–Fe carbonate	218 ± 10 Ma, 62 ± 8.2 Ma	This Study
Sm–Nd	Mn–Fe carbonate	173 ± 7.4 Ma	This Study
Rb–Sr	sphalerite	147.2 ± 3.2 Ma	This Study
Re–Os	Pyrite	47.7 ± 7.9 Ma, 9.0 ± 1.9 Ma	This Study

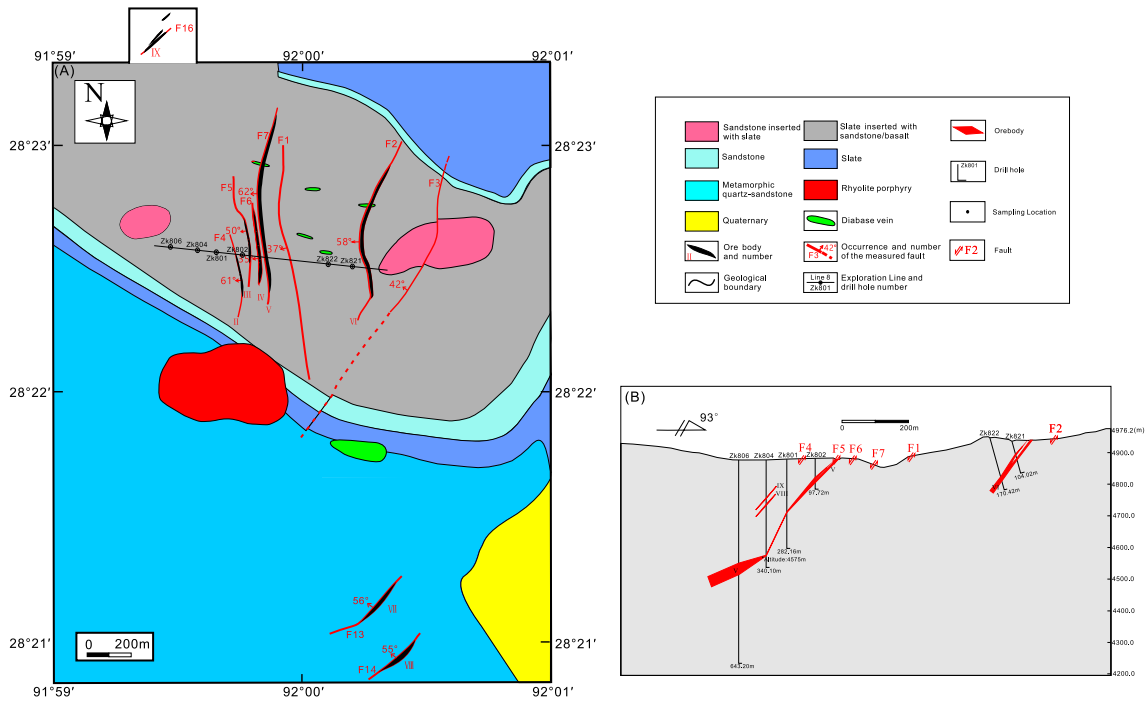

Fig. 2. (A) Geological map of the Zhaxikang Sb–Pb–Zn–Ag polymetallic deposit (modified from Zheng et al, 2012; Wang et al., 2017); (B) Cross-section along the Exploration Line 8.

The regional strata, cropping out in an EW and NWW trend, consists of Precambrian Laguigangri Group and a series of Upper Triassic, Jurassic, Lower Cretaceous, as well as Quaternary sediments. A set of Late Triassic-Early Cretaceous flysch formations formed by turbidity sediment and carbonaceous-siliceous-argillaceous rock series related to hydrothermal sedimentation is in dominance and hosts majority of mineralization in NHMB (Zheng et al., 2012).

The EW-trending faults namely the Lazi-Qiongduojiang, Rongbu-Gudui, and Luozha Faults and the NS-trending faults including the Sangri-Cuona, Yadong-Gulu, Shenzha-Xietongmen and Dangreyongcuo-Gucuo Rift Zones both with multiple episodes of motion occur in NH. Separately, the older EW-trending faults that cover a larger area control the distribution of intermediate-acid magmatic rocks and ore deposits in NHMB (Qiu and Yang, 2011; Zheng et al., 2012). The younger NS-trending faults formed from 25 Ma to now, especially during 18 to 4 Ma (Yin et al., 1999; Williams et al., 2001) are also important ore-controlling structures (Liang et al., 2013) and are considered as the result of east–west extension of the Qinghai-Tibet Plateau (Coleman and Hodges, 1995; Kapp et al., 2008).

The Mesozoic magmatism generated multiple suites of mafic-intermediate igneous rocks including basaltic volcanic interlayers, dyke swarms, and sub-volcanic dykes from Late Triassic to the Early Cretaceous within NH. Among these Mesozoic magmatic rocks, the basic dyke swarms have zircons SHRIMP U–Pb ages of 134.9 ± 1.8 Ma, 135.5 ± 2.1 Ma (Jiang et al., 2007) and 138.0 ± 3.5 Ma (Tong et al., 2007), yet the gabbro show an older zircons SHRIMP U–Pb age of 155.8 Ma (Bian and Ding, 2006). Pan et al. (2006); Zhong et al. (2004) and Tong et al. (2007) regarded these mafic-intermediate igneous rocks as the result of late-stage massive expansion of Neo-Tethys Ocean under the structural environment of the Himalaya passive continental margin intensive stretching and breaking-off, lithosphere extension-thinning and asthenosphere upwelling. On the contrary, Zhu et al. (2009) and Qiu et al. (2010) suggested that these mafic-intermediate igneous rocks are resulting from interaction between mantle plume and Lithospheric mantle material, and form in the continental-rift environment. By contrast, the Cenozoic magmatism is characterized by the formation of monzogranite, leucogranite, diorite, porphyritic diorite, and aplite units (Nie et al., 2005; Zeng et al., 2012). These Cenozoic intermediate-acidic intrusive masses, considered to be the result of crustal thickening (Searle et al., 1997) related to collision of the India and Eurasia Plates during post-collision period (25 to 0 Ma; Harrison et al., 1995; Hou et al., 2006), distribute in the core of Ranba, Kangma and Yelaxiangbo dome as well as EW-trending faults in the form of batholith, laccolith and dykes (Fig. 1C).

2.2. Ore deposit geology

The Zhaxikang deposit is located ~48 km west from Longzi County Town within NHMB (Fig. 1C). In orefield, the Lower Jurassic Ridang

formation consists of epi-metamorphic marine clastic rocks and hosts the majority of mineralization (Fig. 2A). The strata within orefield also include a few Upper Jurassic Weimei formation composed of fine-grained metamorphic quartzose sandstone, silty slate, and calcarenite, as well as Quaternary sediments distributed along valleys (Fig. 2A, Zheng et al., 2012). The magmatism in orefield have generated the magmatic rocks including diabase, porphyritic rhyolite, basalt, and leucogranite units as well as some granite porphyry dykes that intruded into the porphyritic rhyolite (Fig. 2A). According to previous research, the diabase and rhyolite porphyry have zircon SHRIMP U–Pb ages of ~133 Ma (Zheng et al., 2012) and ~135 Ma (Lin et al., 2014), respectively (Table 1). The orefield geological structures are dominated by near NS-striking fault system coexisting with a group of NE-striking faults and some folds (Fig. 2A). Sixteen faults, identified by engineering and geological mapping projects, hosts nine orebodies (Fig. 2). The largest and richest orebody V, where our samples from, hosts more than 80% of the reserves within orefield. The ore-forming elements exhibit a vertical sequence that is zoned from a lowermost Zn (Pb + Ag) zone through a central Zn + Pb + Ag–(Sb) zone to an uppermost Pb + Zn + Sb + Ag zone, whereas no horizontal zoning is present (Wang et al., 2018a). Moreover, various types of alteration associated with mineralization, including the silicification associated with Sb mineralization, carbonatization that is related to Pb–Zn mineralization in the form of Mn–Fe carbonate vein, the chlorite alteration, weak sericite alteration and clay alteration, have occurred in orefield.

Based on hand specimen and microscopic observations, the ore paragenetic sequence in Zhaxikang deposit comprises six stages of ore formation (Fig. 3). These six stages are assigned to three clear pulses: the first pulse is Pb–Zn mineralization and consists of stages 1 and 2, the second pulse is Sb–Ag mineralization and includes stages 3 and 4, and the third pulse is Sb–Hg mineralization including remaining stages (5 and 6). Stage 1 is characterized by a Mn–Fe carbonate + sphalerite + pyrite + arsenopyrite assemblage and the ores show lamellar (Fig. 4A–B), disseminated (Fig. 4C), fine-grained layered and colloform textures (Zheng et al., 2012). Stage 2 is marked by the development of the Mn–Fe carbonate + galena + sphalerite + pyrite ± arsenopyrite assemblage and has massive, banded, net-veined, brecciated, concentric annular, globular, and disseminated ores (Fig. 4D–I). This stage hosts majority of Pb–Zn mineralization. Stage 3 is a transitional stage and mineral assemblages are dominated by quartz ± calcite + pyrite + sphalerite + galena ± chalcopyrite ± arsenopyrite (Fig. 4J–L). The stage 3 sulfides mainly form by the modification of sulfides from earlier stages. Stage 4 comprises an assemblage of quartz + antimony-lead-silver sulfosalt minerals (boulangerite, jamesonite, bournonite, tetrahedrite and andorite) and hosts majority of Sb–Ag mineralization. The ore textures are mainly massive (Fig. 4M–N), vined (Fig. 4J) and needle-like (Fig. 4N). Stage 5 is distinguished by a mineral assemblage composed of quartz + stibnite + cinnabar (Fig. 4O) and hosts part of the Sb mineralization. Stage 6 contains no sulfides and is characterized by quartz-calcite veins that crosscut earlier formed ores (Fig. 4K). The minerals in supergene stage mainly involve ferrohydrite, smithsonite, sardinianite, valentinite, travertine, malachite and siliceous sinter (Fig. 3).

3. Sampling and analytical methods

3.1. Rb–Sr isotopes

The Rb–Sr isotopic analyses were performed on Triton mass spectrometer at the Analytical Laboratory of the Tianjin Institute of Geology and Mineral Resources, Tianjin, China. Five sphalerite samples for Rb–Sr isotopic analyses were separated from stage 2 ores composed of coarse-grained Mn–Fe carbonate and sulfides. These ore samples were crushed to around 20–40 mesh, then the separation and handpicking of sphalerite grains were completed under a binocular microscope, which make the purity more than 98%. The sphalerite grains were washed ultrasonically in analytical-grade alcohol and ultrapure millipore water, and then dissolved in a mixture of 0.3 ml 3 M HNO_3 and 0.1 ml HF at 120 °C. Rb–Sr were separated using ion exchange columns. The Sr fraction was separated following standard chromatographic techniques using AG50x8 and PTFE-HDEHP resins with HCl as the eluent. $^{87}Sr/^{86}Sr$ isotope ratios were normalized to $^{86}Sr/^{88}Sr = 0.1194$. The $^{87}Sr/^{86}Sr$ ratios of NBS987 Sr standard (0.710253 ± 6) match that of Nakai et al. (1989; 0.710242 ± 20) well. For detailed experimental procedures please see Li et al. (2011).

3.2. Re–Os isotopes

The Re–Os isotopes were measured on a negative thermal ionization mass spectrometer (TIMS) at the University of Arizona, Tucson, USA (Creaser et al., 1991). The detailed procedures for sample digestion, column chemistry and instrumental analysis have been described in Mathur et al. (2000). Only a brief description is given below. Ten stages 1 and 2 ore samples (Fig. 5) were crushed and grinded to 80–100 mesh and separates of pyrite crystals were prepared with careful handpicking under a binocular microscope on the basis of size, clarity, color, and morphology to achieve a purity of 99%. Then 0.5–1.5 g of pyrite separates were dissolved in a mixture of HNO_3-HCl within Carius tube. In order to ensure the oxidation of samples and spike equilibration, H_2O_2 was also added (Shirey and Walker, 1995). Os was separated and purified in a two-stage distillation process similar to that described by Frei et al. (1998). Re was extracted and purified through column chemistry. The errors were calculated by varying the concentration of Os blank (0.2 picograms; $^{187}Os/^{188}Os = 0.26$).

3.3. Sm–Nd isotopes

The Sm–Nd isotopic analyses were conducted on VG354 multi collectors mass spectrometer at the Institute of Soil Science, Chinese Academy of Sciences, Nanjing, China. Eleven stages 1 and 2 ore samples for Sm–Nd isotopic analyses were crushed and grinded to 200 mesh, then the sulfides were removed by careful handpicking under a binocular microscope, the purity of Mn–Fe carbonate powders can reach 99%. 0.1 g Mn–Fe carbonate powders were dissolved in a mixture of HF-HNO_3-$HClO_4$. The purified process is completed by ion exchange resin. The whole-process background of Nd is 6×10^{-11} g. The $^{143}Nd/^{144}Nd$ value of standard sample (0.511864 ± 3) accord with that of American La Jolla Nd isotopic standard (0.511860 ± 20). The detailed experimental process is given in Wang et al. (2006).

3.4. U–Pb isotopes and trace elements of zircons

Twelve zircons were separated from Mn–Fe carbonate powders (200 mesh) by conventional heavy liquid and magnetic separation techniques. Then the zircon grains were mounted in epoxy resin and polished to approximately half thickness. In order to check the internal structures of individual zircons and guide U–Pb dating, the Cathodoluminescence (CL) images were taken in Peking University. The U–Pb isotopes and trace elements were analyzed synchronously on Laser-ablation inductively coupled plasma mass spectrometer (LA-ICP-MS) at Wuhan SampleSolution Analytical Technology Co., Ltd, Wuhan, China. The detailed operating conditions for the laser ablation system and ICP-MS instrument, and data reduction are same as description by Liu et al. (2010) and Geng et al. (2017). ICPMSDataCal (Liu et al., 2010) is used to perform the off-line selection, integration of background, analyte signals, time-drift correction and quantitative calibration for trace-element analyses and U–Pb dating. Meanwhile, the ISOPLOT program of Ludwig (Ludwig, 2003) is used for plotting Concordia diagrams and age spectra, as well as age calculations.

4. Results

4.1. Rb–Sr isotopes

The Rb–Sr isotopic data are exhibited in Table 2. The sphalerite samples produce $^{87}Rb/^{86}Sr$ ratios ranging from 0.446 to 2.147 and

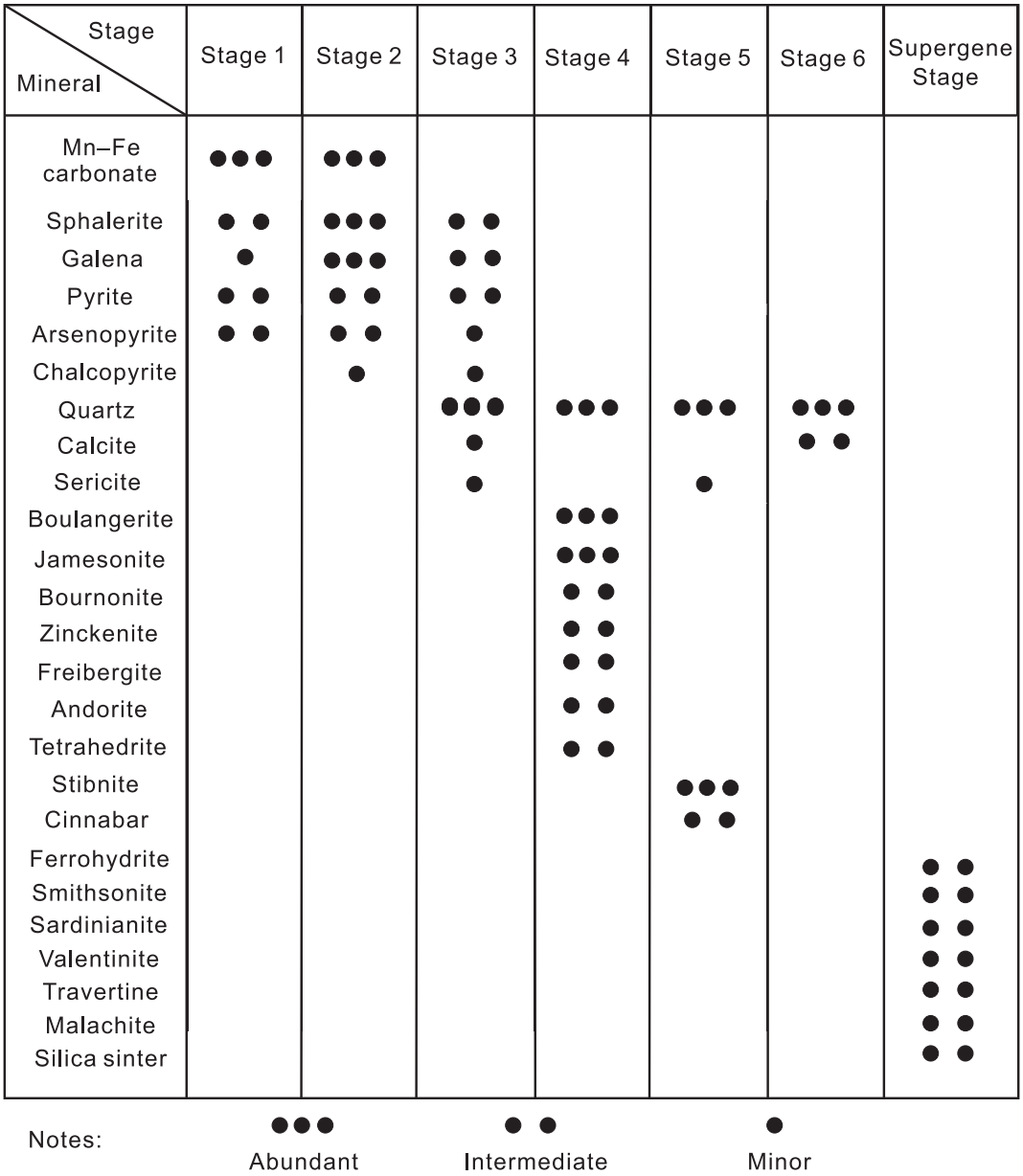

Fig. 3. Ore paragenetic sequence within the Zhaxikang deposit.

$^{87}Sr/^{86}Sr$ ratios ranging from 0.712312 to 0.713189, with Rb and Sr concentrations of 0.0457–0.2214 ppm and 0.274–0.466 ppm, respectively. These Rb–Sr isotopic data (For accurate dating, the sample with highest $^{87}Rb/^{86}Sr$ ratio was rejected for age calculation) define an isochron age of 147.2 ± 3.2 Ma (Fig. 6B; Table 1).

4.2. Re–Os isotopes

The Re–Os isotopic data are listed in Table 3. The pyrite samples have Re concentrations of 0.11–41.78 ppb, Os concentrations of 1–42 ppb, $^{187}Os/^{188}Os$ values of 0.31–32.10 and $^{187}Re/^{188}Os$ values of 145–43489. These pyrite samples are divided into two sets according to mathematical characteristics during data analyses. Detailedly, six samples yield a Re–Os isochron age of 9.0 ± 1.9 Ma (Fig. 7A; Table 1) with lower initial $^{187}Os/^{188}Os$ values (0.25–1.16); another two samples with higher initial $^{187}Os/^{188}Os$ values (4.45 and 4.48) have a slope yielding an age of 47.7 ± 7.9 Ma in "$^{187}Os/^{188}Os$ vs $^{187}Re/^{188}Os$" plot (Fig. 7B).

4.3. Sm–Nd isotopes

The Sm–Nd isotopic data are shown in Table 4. The Mn–Fe carbonate show Sm concentrations of 0.924–5.138 ppm, Nd concentrations of 4.615–12.610 ppm, $^{147}Sm/^{144}Nd$ values of 0.1017–0.6238 and $^{143}Nd/^{144}Nd$ ratios of 0.511756–0.512341 (Table 4). These Sm–Nd isotopic data yield an isochron age of 173 ± 7.4 Ma (Fig. 8B; Table 1).

4.4. U–Pb isotopes and trace elements of zircon

The U–Pb isotopic and trace elemental data are given in Tables 5 and 6, respectively. These long-thin zircons are generally oscillatory zoned (Fig. 9) and exhibit fractionated REE patterns with positive Ce and negative Eu anomalies (Fig. 10). Seven precursor zircons yield a $^{206}Pb/^{238}U$ age of 218 ± 10 Ma (Fig. 11A; Table 1), and another five younger zircons define a $^{206}Pb/^{238}U$ age of 62 ± 8.2 Ma (Fig. 11B; Table 1).

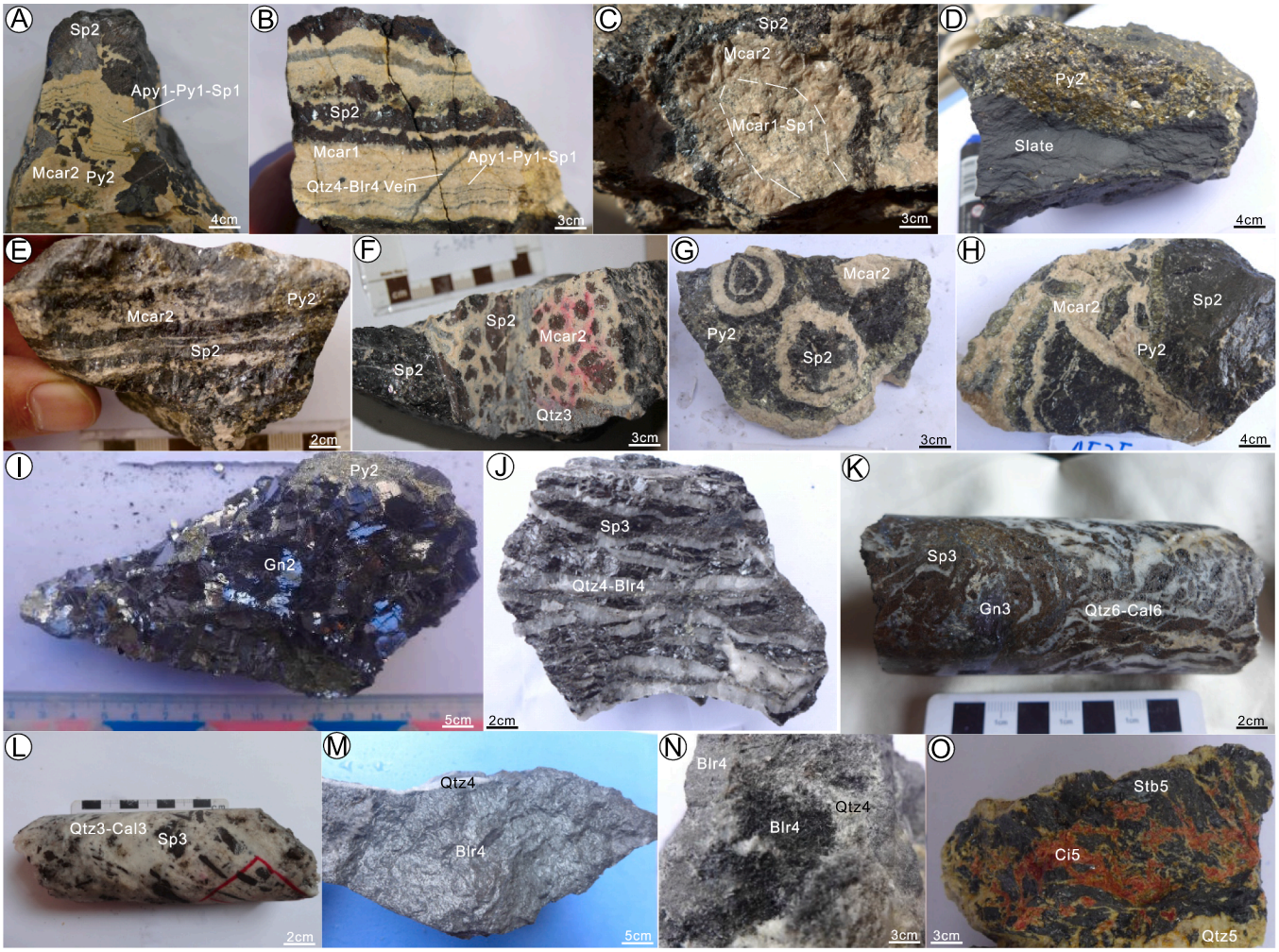

Fig. 4. Hand specimen photographs and photomicrographs of representative samples from the Zhaxikang deposit. (A) Stage 1 lamellar sphalerite-pyrite-arsenopyrite and stage 2 massive sphalerite-pyrite hosted within fine-grained Mn–Fe carbonate. (B) Stage 1 lamellar sphalerite-pyrite-arsenopyrite and stage 2 massive sphalerite-pyrite hosted within fine-grained Mn–Fe carbonate. (C) Coarse-grained stage 2 Mn–Fe carbonate-sphalerite formed by the recrystallization of fine-grained stage 1 Mn–Fe carbonate-sphalerite. (D) Stage 2 massive coarse-grained pyrite hosted by slate. (E) Stage 2 coarse-grained sphalerite-pyrite hosted by stage 2 Mn–Fe carbonate with banded textures. (F) Stage 2 sphalerite and Mn–Fe carbonate ore with typical Dal Matianite texture. (G) Stage 2 massive, globular and concentric annular sphalerite-pyrite hosted by coarse-grained Mn–Fe carbonate. (H) Stage 2 massive and veined sphalerite-pyrite hosted by coarse-grained Mn–Fe carbonate. (I) Stage 2 massive galena and pyrite. (J) Stage 3 sphalerite cross-cut by stage 4 quartz-boulangerite veins. (K) Stage 3 sphalerite-galena veins cross-cut by stage 6 quartz-calcite veins. (L) Stage 3 brecciated sphalerite within stage 3 quartz-calcite. (M) Stage 4 boulangerite-quartz. (N) Stage 4 massive and needle-like boulangerite hosted by stage 4 quartz. (O) Stage 5 stibnite-cinnabar hosted by stage 5 quartz. Abbreviations are as follows: Mcar1 = stage 1 fine-grained Mn–Fe carbonate; Apy1 = stage 1 lamellar arsenopyrite; Py1 = stage 1 lamellar pyrite; Sp1 = stage 1 lamellar sphalerite; Mcar2 = stage 2 coarse-grained Mn–Fe carbonate; Py2 = stage 2 pyrite; Sp2 = stage 2 sphalerite; Gn2 = stage 2 coarse-grained galena; Py3 = stage 3 pyrite; Sp3 = stage 3 sphalerite; Gn3 = stage 3 galena; Qtz3 = stage 3 quartz; Cal3 = stage 3 calcite; Blr4 = stage 4 boulangerite; Qtz4 = stage 4 quartz; Stb5 = stage 5 stibnite; Qtz5 = stage 5 quartz; Ci5 = stage 5 cinnabar; Cal6 = stage 6 calcite; Qtz6 = stage 6 quartz.

5. Discussion

5.1. Multiple isotopic geochronological evidence

5.1.1. Rb–Sr isochron age of sphalerite

Traditionally, Pb–Zn deposits are difficult to date accurately owing to the absence of suitable minerals or dating methods. Rb–Sr dating of sphalerite has been demonstrated as a feasible method. However, the uncertainty over exact host phases for the trace amounts of Rb–Sr and causes of Rb/Sr variability have caused concern in reliability of this method (Christensen et al., 1995). The inherited inclusions within sphalerite may lead to the Rb–Sr data not forming isochrons or forming meaningless isochrons (Nakai et al., 1993). Pure sphalerites commonly have much higher Rb/Sr ratios than their host fluid inclusions, and sphalerites with high Rb/Sr ratios and Sr concentrations often yield well-constrained isochron ages due to not significantly influence by host fluid inclusions.

Several successful examples have been reported. For instance, Nakai et al. (1990) reported Rb–Sr isochron age (377 ± 29 Ma) of sphalerite from Tennessee Pb–Zn deposit to rule out any genetic connection with the Alleghenian orogeny (330–250 Ma) and confirm the association between MVT mineralization and older Acadian orogeny (380–350 Ma). Then, Nakai et al. (1993) investigated Rb–Sr isotopes of sphalerite from Pine Point Pb–Zn ore district and the Rb-Sr age (361 ± 13 Ma) indicated that the mineralization took place shortly after deposition of the middle Devonian host carbonate rocks, which implied the MVT genesis and excluded the mineralization models related to early Tertiary Cordilleran deformation evidenced by regional fluid migration. Christensen et al. (1995) also showed Rb–Sr isochron age (366 ± 15 Ma) of sulfides from Polaris MVT deposit that is hosted in significantly older sedimentary rocks and has geologically well-constrained age of formation confirmed by paleomagnetic measurements, which provide the first unequivocal vindication of the reliability of this method. Moreover, Ostendorf et al.

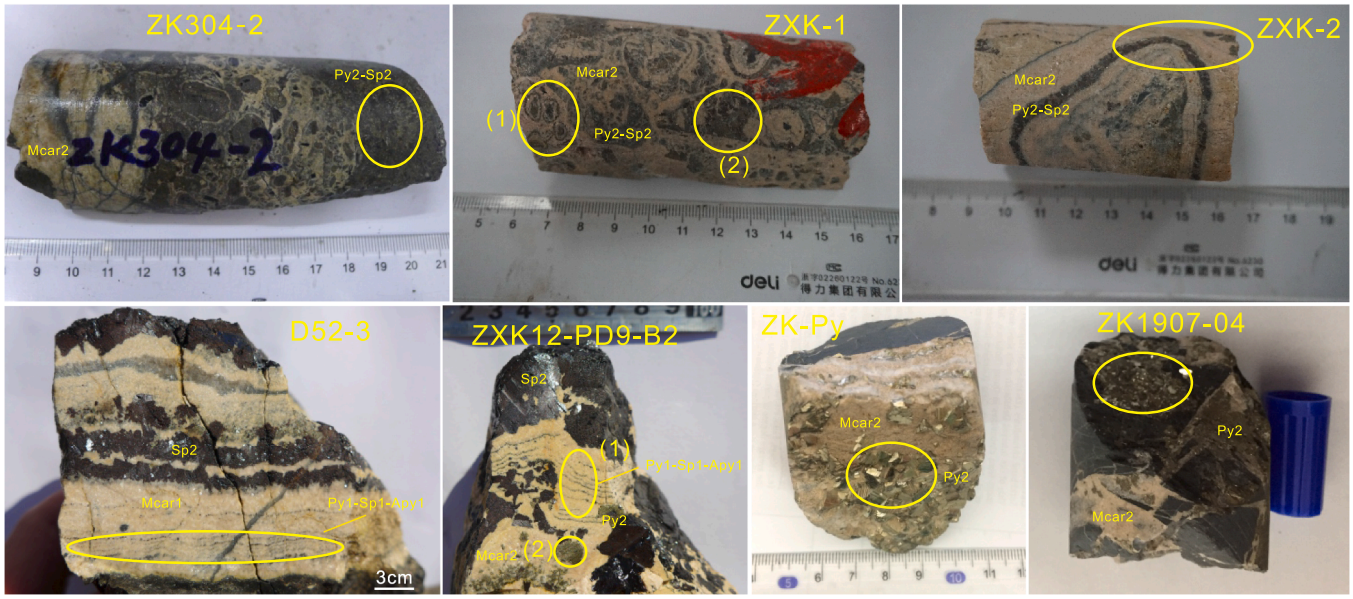

Fig. 5. (A) Hand specimen photographs of the samples for Re–Os isotopic analyses, the ovals represent the sampling area. Abbreviations are as Fig. 4.

Table 2
The Rb–Sr isotopic data for stage 2 sphalerite from Zhaxikang deposit.

Sample Number	Rb (ppm)	Sr (ppm)	$^{87}Rb/^{86}Sr$	$^{87}Sr/^{86}Sr$	2σ
ZXK12-B14-3	0.0809	0.466	0.502	0.712628	0.000012
ZXK12-B16-2	0.0457	0.297	0.446	0.712519	0.000012
ZXK12-B16-4	0.0498	0.308	0.468	0.712563	0.000010
ZXK12-B34-2	0.0727	0.274	0.768	0.713189	0.000008
ZXK12-B14-1	0.2214	0.298	2.147	0.712312	0.000014

(2015, 2017) studied Rb-Sr isotopic geochronology of sphalerite from Jabali Zn–Pb–(Ag) deposit in Yemen (144.0 ± 4.3 Ma) and Tres Marias Zn–Pb–(Ge) deposit in Mexico (28.8 ± 1.7 Ma), and then revealed their MVT and carbonate-hosted geneses, respectively.

With the regards to Zhaxikang deposit, four sphalerite samples produce $^{87}Rb/^{86}Sr$ ratios that range from 0.446–0.768 and Sr concentrations that range from 0.274–0.466 (Table 2), except one sample with the highest $^{87}Rb/^{86}Sr$ ratio (2.147) that may be influenced by later mineralization events. These Rb–Sr isotopic characteristics of sphalerite samples in Zhaxikang deposit are similar to those of sphalerite from Pine Point Pb-Zn ore district ($^{87}Rb/^{86}Sr$: 0.61–8.40, Sr concentrations: 0.05–0.35; Nakai et al., 1993) and Polaris MVT deposit ($^{87}Rb/^{86}Sr$: 0.17–1.96, Sr concentrations: 0.08–1.04; Christensen et al., 1995). Meanwhile, the non-linear relationship between $^{87}Sr/^{86}Sr$ ratios and 1/Sr (Fig. 6A) indicates that the isochron is not produced by two-component mixing (Pettke and Diamond, 1996). Therefore, these Rb–Sr isotopic data could define a good isochron age (147.2 ± 3.2 Ma; Fig. 6B; Table 1).

5.1.2. Re–Os isochron ages of pyrite and reset of earlier Re–Os isotopic system

The Re–Os isotopes are useful for timing and providing genetic information for ore deposits as Re and Os concentrate in sulfide minerals rather than associated alteration minerals. Due to that Re is more incompatible than Os during mantle melting, the crustal materials usually have a larger Re/Os ratio and higher $^{187}Os/^{188}Os$ ratios than mantle (Walker et al., 1989). Therefore, the Os source can be used to distinguish crustal and mantle reservoirs involved in ore formation (Mathur et al., 2002). Mathur et al. (2002) determined the Re–Os ages of molybdenite (114.2 ± 0.6 Ma and 115.2 ± 0.6 Ma) to constrain on the mineralization age of Candelaria Fe Oxide Cu-Au deposit in Chile and to explore possible genetic links with the batholithic intrusions in the area. Similarly, Qiu et al. (2014) also used the Re–Os ages of molybdenite (212.7 ± 2.6 Ma and 215.1 ± 2.6 Ma) to reveal the relation between Mo mineralization and granitic magmatism.

As for Zhaxikang deposit, the pyrite samples show no significant difference in geological characteristics (Fig. 5). Although the single point age of pyrite samples is usually considered have no referential

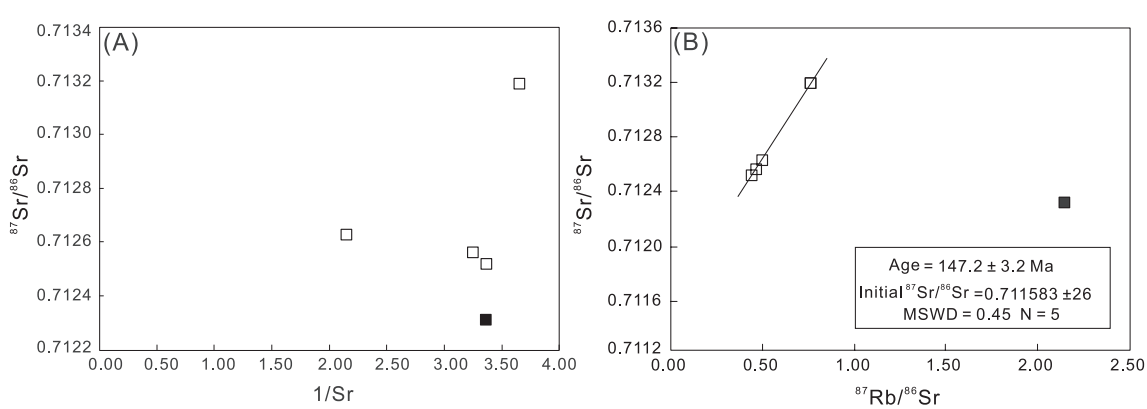

Fig. 6. (A) The $^{87}Sr/^{86}Sr$ vs. 1/Sr plot of stage 2 sphalerite from the Zhaxikang deposit; (B) The Rb–Sr isochron age of stage 2 sphalerite from the Zhaxikang deposit. One solid data point was rejected for age calculation.

Table 3
The Re–Os isotopic data for stages 1 and 2 pyrite from Zhaxikang deposit.

Sample Number	Re (ppb)	Os (ppb)	$^{187}Os/^{188}Os$	error	$^{187}Re/^{188}Os$	error	Initial $^{187}Os/^{188}Os$
ZXK12-PD9-B2-1	28.50	35	32.10	1.60	34733	2084	4.45
D52-3	17.80	42	5.80	0.30	35323	1766	0.47
ZXK12-PD9-B2-2	4.10	3	7.54	0.40	43489	2147	0.97
ZXK-2	0.22	4	0.31	0.22	410	21	0.25
ZK1907-04	0.32	17	4.60	0.20	145	7	4.48
9-4	6.24	–	–	–	–	–	
ZXK-1(2)	41.78	–	–	–	–	–	
ZXK-1(1)	0.11	1	1.47	0.10	2047	184	1.16
ZK304-2	0.62	1	2.20	0.10	9471	568	0.77
ZK-Py	18.20	41	5.70	0.30	34947	3145	0.42

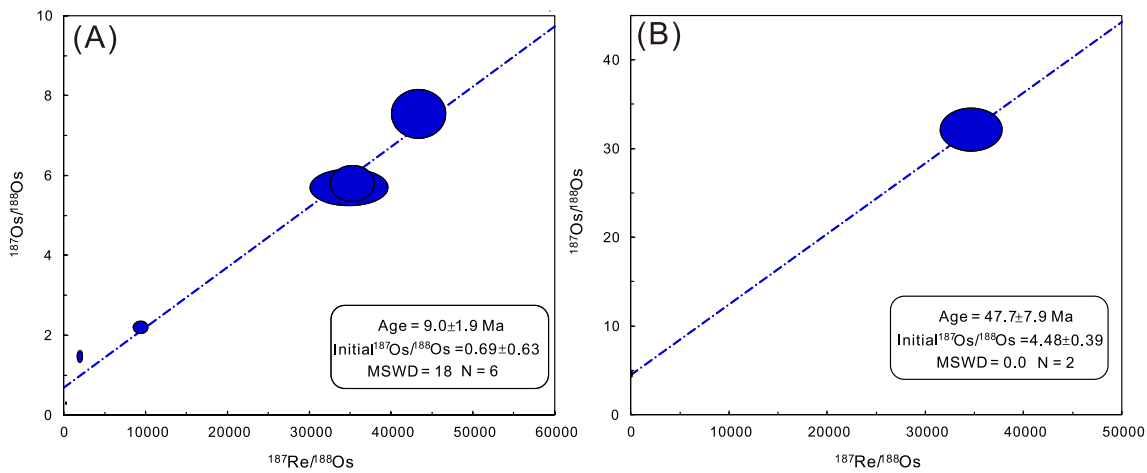

Fig. 7. (A) The Re–Os isochron age (9.0 ± 1.9 Ma) of six pyrite samples from the Zhaxikang deposit; (B) Another two samples have a slope yielding an age of 47.7 ± 7.9 Ma.

meaning, it can also reflect some facts. The single point ages of two samples are obvious older than other six samples in Zhaxikang deposit. Thus, these eight pyrite samples are divided into two sets according to mathematical characteristics during data analyses. Detailedly, six samples yield a Re–Os isochron age of 9.0 ± 1.9 Ma (Fig. 7A; Table 1) with lower initial $^{187}Os/^{188}Os$ values (0.25–1.16). Another two samples with higher initial $^{187}Os/^{188}Os$ values (4.45 and 4.48) have a slope yielding an age of 47.7 ± 7.9 Ma in"$^{187}Os/^{188}Os$ vs $^{187}Re/^{188}Os$"plot (Fig. 7B), this age should have some referential meaning as it's similar to previous Re–Os isochron age (43.1 ± 2.5 Ma) of sulfides from Zhaxikang deposit (Zhou et al., 2018; Table 1). Additionally, the pyrite samples have higher initial $^{187}Os/^{188}Os$ values (0.25–4.48) than mantle source (0.13; Meisel et al., 1996) and larger Re/Os ratios (0.73–53.13), which suggest the ore-forming metals should have crustal origins. The crustal origins for ore-forming metals are also proved by previous Pb isotopic evidence (Sun et al., 2018; Zhou et al., 2018). Nevertheless, the more radiogenic initial $^{187}Os/^{188}Os$ values of two older pyrite samples (4.45 and 4.48) than other younger six pyrite samples (0.25–1.16) reveal that these two sets of sulfides have different Os sources and the two older samples require a more significant contribution of crustal Os to related ore-forming hydrothermal system.

On the other hand, previous research suggests that alteration by later ore-forming fluids with different temperature and salinity could change and reset Re–Os isotopic system of earlier sulfides (McCandless et al., 1993; Mathur et al., 2000; Suzuki et al., 2000). There are following facts in Zhaxikang deposit: (1) from stages 1 and 2 (220–240 °C, 12–15 wt% NaCl equiv.) through stages 3 and 4 (220–310 °C, 6–10 wt% NaCl equiv.) to stages 5 and 6 (230–270 °C, 3–10 wt% NaCl equiv.), the temperature and salinity of ore-forming fluids obviously changed according to fluid inclusions data (Yu, 2015); (2) although the pyrite samples are all from early Pn–Zn mineralization and have no significant difference in geological characteristics (Fig. 5), they are divided into

Table 4
The Sm–Nd isotopic data for Mn–Fe carbonate from Zhaxikang deposit.

Sample Number	Sm (ppm)	Nd (ppm)	$^{147}Sm/^{144}Nd$	$^{143}Nd/^{144}Nd$	2σ
ZXK-12-B14	2.791	8.365	0.2018	0.511862	0.000007
ZXK-12-B16	1.235	4.901	0.1523	0.511804	0.000009
ZXK-12-B158	1.067	4.615	0.1398	0.511785	0.000006
ZXK-12-B34	2.948	8.659	0.2064	0.511887	0.000010
ZXK-12-B8	4.016	12.610	0.1929	0.511823	0.000011
ZXK-12–B13	3.843	5.385	0.4317	0.512121	0.000009
ZK005-B4(517 m)	2.402	6.764	0.2149	0.511876	0.000008
ZK006-B6(615 m)	3.675	6.423	0.3461	0.512024	0.000007
ZXK-12-B13-1	5.138	4.986	0.6238	0.512341	0.000008
ZXK-12-B13-2	0.924	5.493	0.1017	0.511756	0.000007
ZK006-B6(615 m)-1	4.826	5.129	0.5695	0.512279	0.000009

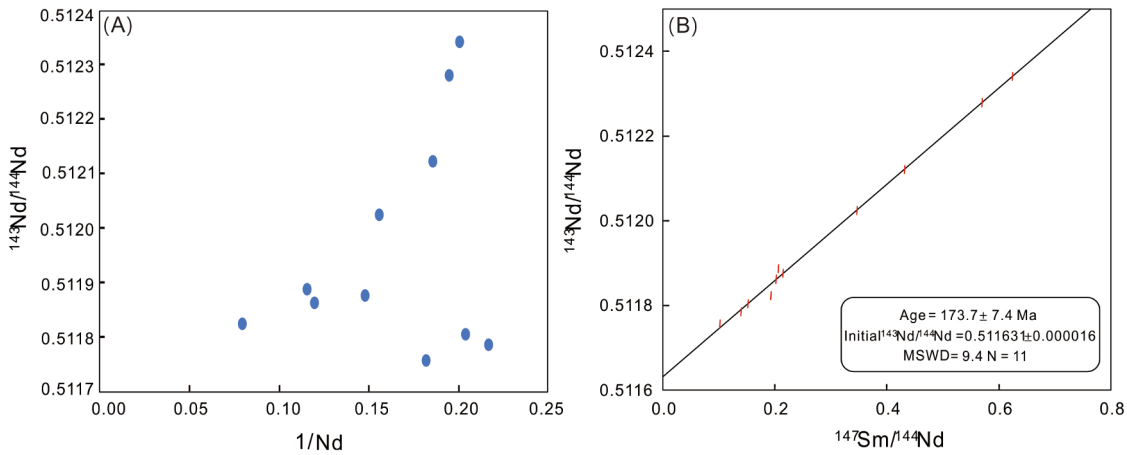

Fig. 8. (A) The $^{143}Nd/^{144}Nd$ vs. 1/Nd plot of Mn–Fe carbonate from the Zhaxikang deposit; (B) The Sm–Nd isochron age of Mn–Fe carbonate from the Zhaxikang deposit.

two sets according to mathematical characteristics during data analyses and yield different Re–Os ages (47.7 ± 7.9 and 9.0 ± 1.9 Ma); (3) the pyrite show much younger ore-forming ages (Re–Os ages: 47.7 ± 7.9 and 9.0 ± 1.9 Ma; Fig. 7) than coexisting Mn–Fe carbonate (Sm–Nd age:173.7 ± 7.4 Ma; Fig. 8) and sphalerite (Rb–Sr age:147 ± 3.2 Ma; Fig. 6); (4) because of the chalcophile and siderophile nature of Re–Os, the pyrite is dominated Re–Os-bearing sulfides in Zhaxikang deposit, and the limited amounts of pyrite make its Re–Os system easily to be reset. To conclude, there should be at least two later mineralization events with crustal origins randomly reset the Re–Os isotopic system of earlier sulfides from Pb–Zn mineralization. However, the particular resetting mechanism need further research.

5.1.3. Sm–Nd isochron age of Mn–Fe carbonate

The Sm–Nd isotopic geochronology of carbonate is also widely applied to determine mineralization age. For example, Su et al. (2009) analyzed Sm–Nd isotopes of hydrothermal calcites to determine the gold deposition age of Shuiyindong Carlin-type gold deposit in China. In Zhaxikang deposit, there are plenty of Mn–Fe carbonate coexisting with sulfides (e.g., pyrite, arsenopyrite, sphalerite and galena), so the Sm–Nd isotopic geochronology research of Mn–Fe carbonate can also provide credible evidence for mineralization age. Be similar to Rb–Sr isotopes, we exclude the possibility that the isochron is produced by two-component mixing by the non-linear relationship between $^{143}Nd/^{144}Nd$ ratios and 1/Nd (Fig. 8A). Therefore, the Sm–Nd isochron age (173 ± 7.4 Ma; Fig. 8B) can represent the forming ages of Mn–Fe carbonate.

5.1.4. $^{206}Pb/^{238}U$ ages and origin of zircons in Mn–Fe carbonate

The zircon U–Pb isotopic geochronology is another most common dating method in hydrothermal ore deposit study and corresponding geodynamic evolution (Qiu et al., 2016; Qiu and Deng, 2017). To Zhaxikang deposit, as mentioned in Section 4.4, the long-thin zircons in Mn–Fe carbonate are generally oscillatory zoned (Fig. 9) and exhibit fractionated REE patterns with positive Ce and negative Eu anomalies (Fig. 10), which indicate they are magmatic zircons (Hoskin and Schaltegger, 2003; Wu et al., 2018). However, in "La vs $(Sm/La)_N$" and "$(Sm/La)_N$ vs δCe" plots (Fig. 12), both precursor ($^{206}Pb/^{238}U$ age: 218 ± 10 Ma) and younger ($^{206}Pb/^{238}U$ age: 62 ± 8.2 Ma) zircons show transforming trend from magmatic to hydrothermal zircon, yet the REE characteristics show that the younger group of zircons experienced more intense hydrothermal activity (Fig. 10), which suggest that these zircons must have been influenced by hydrothermal activity to different degrees. The obvious recrystallization phenomenon of some Mn–Fe carbonate samples (Fig. 4C; Wang et al., 2017) also evidence this inference. In addition, the Sm–Nd isochron age of Mn–Fe carbonate (173 ± 7.4 Ma; Fig. 8B) are younger than the $^{206}Pb/^{238}U$ age of precursor zircons (218 ± 10 Ma; Fig. 11A) but older than the $^{206}Pb/^{238}U$ age of the younger zircons (62 ± 8.2 Ma; Fig. 11B). From the above, we argue that the precursor zircons in Mn–Fe carbonate are most likely inherited zircons captured from wall rocks, and during later hydrothermal activity, the hydrothermal fluid brought the younger magmatic zircons from wall rocks and magmatic rocks into Mn–Fe carbonate in recrystallization process.

5.2. Comparison of geochronological data and regional mineralization events

According to the analytical results in this study and previous geochronological data (Ar–Ar isochron age: 19.3 ± 1.1 Ma; Sun et al., 2018; ESR (electron spin resonance) ages: 18.3 ± 1.8 Ma, 20.3 ± 2.3 Ma; Zhang, 2010; Table 1), there is a discordance of different geochronological data and the ages are very scattered. Meanwhile, we need to consider following facts in Zhaxikang deposit: (1) the ore paragenetic sequence are obvious assigned into three pulses; (2) the early formed ore samples are modified by later mineralization; (3) the mineral association and ore texture of three pulses of mineralization are significantly different. From the above evidence, we hold the opinion that Zhaxikang deposit is a superimposed deposit with three pulses of mineralization and the complicated superimposed mineralization results in the discordance of different methods. Therefore, the scattered geochronological data should be also divided into three periods that is corresponding to three regional mineralization events. In the case of that there is no more suitable minerals or dating methods to date the mineralization ages, these geochronological data should have referential meaning and are enough to demonstrate the exist of three pulses of mineralization in Zhaxikang deposit.

Firstly, the regional strata are dominated by a set of Late Triassic-Early Cretaceous flysch formations formed by turbidity sediment and carbonaceous-siliceous-argillaceous rock series related to hydrothermal sedimentation. This set of rock formation also contains some marine volcanic rocks (Zheng et al., 2014). Comparing with isotopic geochronology data, the $^{206}Pb/^{238}U$ age (218 ± 10 Ma; Fig. 11A) of older zircons in Mn–Fe carbonate match the age of basic volcanic rock intercalation in Upper Triassic Nieru and Lower Jurassic Ridang formations well (around 220–190 Ma; Zheng et al., 2012), which suggest that older zircons may derive from seafloor volcanism; the Sm–Nd isochron age of Mn–Fe carbonate is 173.7 ± 7.4 Ma (Fig. 8B) that is similar to the age of submarine volcanic formation consisting of basalt and andesite in Middle Jurassic Zhela formation (around 180–160 Ma; Zheng et al., 2012); and the Rb–Sr isochron age (147 ± 3.2 Ma; Fig. 6) of stage 2 sphalerite approximate the age of basalt in Upper Jurassic-Lower Cretaceous Sangxiu formation (around 150–130 Ma; Zheng et al.,

Table 5
The U–Pb isotopic data for zircons within Mn–Fe carbonate from Zhaxikang deposit.

Sample Number	Pb (ppm) Total	U (ppm)	Th (ppm)	Th/U	$^{207}Pb/^{206}Pb$	error	$^{207}Pb/^{235}U$	error	$^{206}Pb/^{238}U$	error	$^{207}Pb/^{206}Pb$ Age (Ma)	error	$^{207}Pb/^{235}U$ Age (Ma)	error	$^{206}Pb/^{238}U$ Age (Ma)	error
ZXK-1-05	493.55	3485.20	3575.38	1.03	0.06112	0.00294	0.26701	0.01291	0.03164	0.00054	642.6	71.3	240.3	10.3	200.8	3.4
ZXK-1-07	57.40	639.11	246.74	0.39	0.05138	0.00383	0.25275	0.01800	0.03575	0.00068	257.5	172.2	228.8	14.6	226.4	4.3
ZXK-1-17	258.78	2467.69	1113.43	0.45	0.05999	0.00303	0.31980	0.01729	0.03792	0.00064	611.13	104.6	281.8	13.3	239.9	4.0
ZXK-1-23	255.75	2779.63	974.63	0.35	0.06284	0.00288	0.29734	0.01350	0.03417	0.00048	701.86	93.5	264.3	10.6	216.6	3.0
ZXK-1-28	334.02	3219.86	1589.12	0.49	0.05957	0.00268	0.28417	0.01261	0.03464	0.00055	587.1	98.1	254.0	10.0	219.5	3.4
ZXK-1-29	91.63	1088.94	405.64	0.37	0.05059	0.00267	0.23886	0.01254	0.033954	0.00050	233.4	122.2	217.5	10.3	215.2	3.1
ZXK-2-06	26.15	568.61	615.08	1.08	0.08698	0.01043	0.08806	0.00725	0.00857	0.00030	1361.1	233.3	85.7	6.8	55.0	1.9
ZXK-2-23	24.23	543.11	604.60	1.11	0.06359	0.01140	0.06140	0.00760	0.00821	0.00033	727.8	419.4	60.5	7.3	52.7	2.1
ZXK-2-35	276.17	1855.66	1406.54	0.76	0.06317	0.00310	0.30587	0.01510	0.03480	0.00053	722.2	105.5	271.0	11.7	220.5	3.3
ZXK-2-44	59.864	1135.31	1007.58	0.89	0.06325	0.00556	0.08977	0.00740	0.01049	0.00022	716.7	188.9	87.3	6.8	67.3	1.4
ZXK-2-49	66.78	1173.75	1128.5983	0.96	0.06527	0.00575	0.09737	0.00843	0.01087	0.00023	783.3	189.8	94.3	7.8	69.7	1.5
ZXK-2-74	313.48	10654.27	6259.76	0.59	0.05477	0.00238	0.06951	0.00311	0.00925	0.00017	466.7	98.1	68.2	2.9	59.3	1.1

Table 6
The trace elemental data for zircons within Mn–Fe carbonate from Zhaxikang deposit.

Sample Number	SiO_2	P	Ti	Y	Nb	La	Ce	Pr	Nd	Sm	Eu	Gd	Tb	Dy	Ho	Er	Tm	Yb	Lu	Hf	Ta
ZXK-1-05	94.08	1395.29	24.68	3677.20	4.33	0.77	152.01	3.61	39.87	81.12	28.72	217.38	48.23	395.33	104.97	411.87	82.38	844.05	179.41	32950.95	0.88
ZXK-1-07	95.78	565.42	7.69	2482.91	2.56	0.06	4.76	0.17	3.76	7.64	1.10	50.67	16.47	212.97	79.97	387.76	80.08	862.77	168.06	29171.75	1.53
ZXK-1-17	94.67	1139.70	2.23	4641.14	7.71	0.18	30.60	0.41	4.18	10.99	2.57	72.04	27.75	358.86	141.63	707.73	157.89	1740.72	358.14	30400.17	3.28
ZXK-1-23	94.19	792.93	13.26	4465.14	10.14	0.41	12.27	0.35	6.88	12.05	1.81	77.28	26.68	347.29	139.39	682.72	149.22	1597.36	316.59	35294.12	4.57
ZXK-1-28	94.17	1029.42	14.61	6098.47	19.96	0.28	21.97	0.50	6.29	19.39	3.65	115.78	40.14	517.20	189.48	882.80	176.46	1761.05	338.59	31357.06	6.88
ZXK-1-29	95.32	597.93	13.48	3378.68	4.14	0.25	6.90	0.49	4.57	9.46	1.30	64.75	22.88	284.54	109.35	517.64	108.51	1122.69	215.65	30768.51	2.09
ZXK-2-06	95.28	931.82	45.26	2174.10	4.77	0.05	66.07	0.17	4.42	7.52	1.80	47.78	14.54	181.07	66.23	314.96	65.84	704.76	131.51	32985.51	2.40
ZXK-2-23	95.82	1390.34	52.54	2511.35	4.10	5.13	66.24	1.67	13.26	9.82	2.12	55.43	16.12	201.82	73.07	366.17	75.92	790.27	157.55	27057.92	2.08
ZXK-2-35	94.54	667.84	12.20	3376.93	7.80	2.40	95.50	1.03	10.59	18.35	5.64	72.19	22.42	278.39	105.19	497.83	115.73	1214.83	246.57	34938.87	4.10
ZXK-2-44	94.75	1005.28	17.58	3459.36	13.87	0.00	63.09	0.50	6.73	12.58	1.19	82.11	26.37	319.44	121.38	531.15	110.47	1019.87	189.91	34047.74	5.37
ZXK-2-49	94.27	946.96	3.23	5618.49	8.96	0.09	55.61	0.52	12.20	29.63	2.76	150.58	45.87	529.39	194.97	851.82	171.24	1558.88	290.32	34336.43	4.42
ZXK-2-74	89.10	2970.11	1.09	15574.07	95.71	0.08	39.98	0.18	5.36	27.20	0.47	223.51	93.64	1238.45	495.30	2252.63	455.98	4214.73	769.76	43197.21	28.87

Notes: The unit is % for SiO_2 and ppm for trace elements.

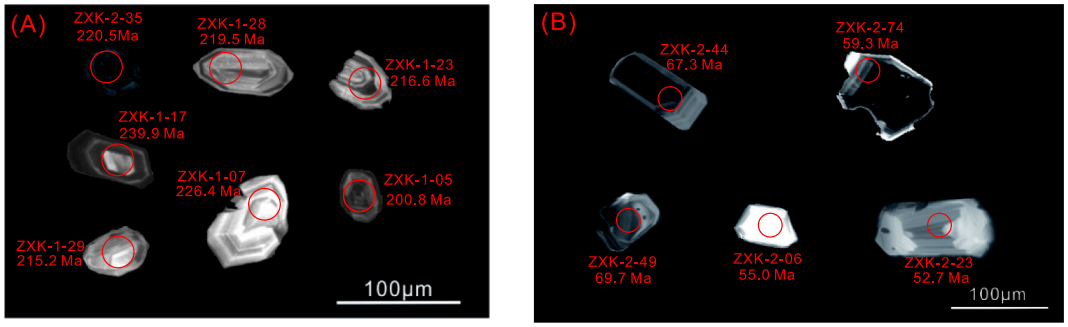

Fig. 9. CL images and the $^{206}Pb/^{238}U$ ages of zircons separated from Mn–Fe carbonate in Zhaxikang deposit. The circles represent the dating locations.

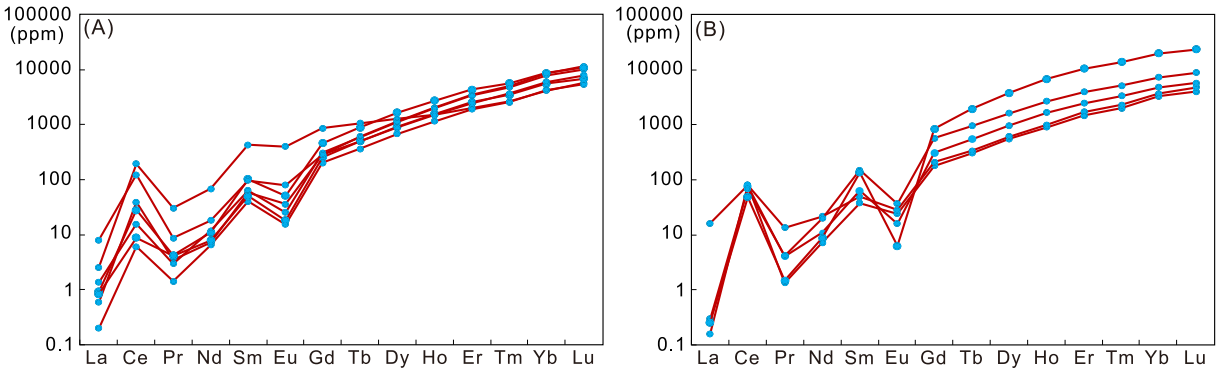

Fig. 10. Chondrite-normalized (McDonough and Sun, 1995) REE diagram for zircons from Mn–Fe carbonate in Zhaxikang deposit. (A) The older group (218 Ma); (B) The younger group (62 Ma).

2012). As a whole, the $^{206}Pb/^{238}U$, Sm–Nd and Rb–Sr isochron ages of early minerals from Pb–Zn mineralization (stage 1 and 2) are consistent with three extensive regional seafloor volcanic events during synsedimentary period (220–130 Ma; Zheng et al., 2014), respectively. Meanwhile, the ores from Pb–Zn mineralization (stages 1 and 2) exhibit the lamellar (Fig. 4A–B), disseminated (Fig. 4C), banded (Fig. 4E), concentric annular (Fig. 4G) and Dal Matianite (Zheng et al., 2012) textures, as well as fine-grained layered and colloform textures with synsedimentary features (Wang et al., 2018a), which are similar to those of the Red Dog SEDEX-type ore district in Alaska (Moore et al., 1987; Leach et al., 2010). Thus, the early Pb–Zn mineralization (stages 1 and 2) in Zhaxikang deposit should be related to multiple seafloor volcanic events during synsedimentary period with submarine hydrothermal sedimentation (metasomatism) genesis.

Secondly, five younger zircons yield the $^{206}Pb/^{238}U$ age of 62 ± 8.2 Ma (Fig. 11B). Meanwhile, two pyrite samples define a Re–Os age (47.7 ± 7.9 Ma; Fig. 7B) that is similar to Zhou et al. (2018; 43.1 ± 2.5 Ma; Table 1). These younger $^{206}Pb/^{238}U$ and older Re–Os ages are in accord with the formation age of regional orogenic Au–Sb deposits formed during syn-collision period of India-Eurasia Plate (60–42 Ma; Zheng et al., 2014). During this period, there are a series of ductile shearing, thrusting nappe and dynamo thermal flow metamorphism within NHMB, which drive the mixing of deep-sourced mantle fluid from mantle exhaust and CO_2-riching fluid from dehydration of lower crust. Then the mixing metamorphic fluid system upwelling along the shear zone to form these Au–Sb deposits. Usually, there would be extensive magmatic activity during orogeny that provide metallogenic metals for metamorphic fluid system to form orogenic deposits (Chen, 2006), which can well explain the exist of younger magmatic zircons in Mn–Fe carbonate ($^{206}Pb/^{238}U$ ages age: 62 ± 8.2 Ma; Fig. 9B and Fig. 11B). In addition, as is well-known, the ore-forming fluids for orogenic Au–Sb deposits should have significant crustal origin (Chen, 2006), which is in keeping with the inference in Section 5.1.2 by Os isotopes that the sample with older Re–Os age (47.7 ± 7.9 Ma; Fig. 7B) require a more significant crustal contribution to related ore-forming hydrothermal system. From above, the metamorphic fluid system related to orogenic Au–Sb deposits during syn-collision period (60–42 Ma) overprinted the Pb–Zn mineralization and formed stages 3 and 4 mineral assemblages in Zhaxikang deposit. The newly found independent gold ore body in Zhaxikang deposit can also confirmed exist of the second pulse of mineralization.

Lastly, the Ar–Ar isochron age of sericite in stage 5 quartz-pyrite-stibnite vein is 19.3 ± 1.1 Ma (Sun et al., 2018; Table 1), which approximate ESR ages (18.3 ± 1.8 Ma, 20.3 ± 2.3 Ma; Table 1) of quartz samples from stage 5 quartz-stibnite veins in Zhaxikang deposit (Zhang, 2010). Meanwhile, another 6 pyrite samples yield a younger Re–Os isochron age of 9.0 ± 1.9 Ma (Fig. 7A). These Ar–Ar and Re–Os isochron, and ESR ages are consistent with the regional mineralization event during post-collision period (25 Ma to now; Zheng et al., 2014). This mineralization event, associated with magmatic-hydrothermal activity involving leucogranite (Li et al., 2017), formed a series of SnW → PbZnAg → AuSb deposits in NHMB. Moreover, this magmatic-hydrothermal mineralization event can also provide crustal Os source to satisfy the six younger pyrite samples (Re–Os isochron age: 9.0 ± 1.9 Ma; Fig. 7A) to have high crustal $^{187}Os/^{188}Os$ values (0.25–1.16) as mentioned in Section 5.1.2. Summing up above evidence, the latest mineralization (stage 5 and 6) in Zhaxikang deposit should relate to magmatic-hydrothermal activity and also overprint earlier mineralization.

5.3. Ore-forming model

The isotopic geochronology evidence reveal that Zhaxikang deposit is a superimposed deposit that dominantly experienced three pulses of mineralization corresponding to three regional mineralization events. The ore-forming model is as follow (Fig. 13; Wang et al., 2018b): (1) the first pulse of mineralization (stages 1 and 2): during synsedimentary period (220–130 Ma), under the influence of multiple seafloor volcanic events, the reducing environment in rifts and adsorption of organic matter lead to the enrichment of metallogenic elements (e.g., Pb, Zn,

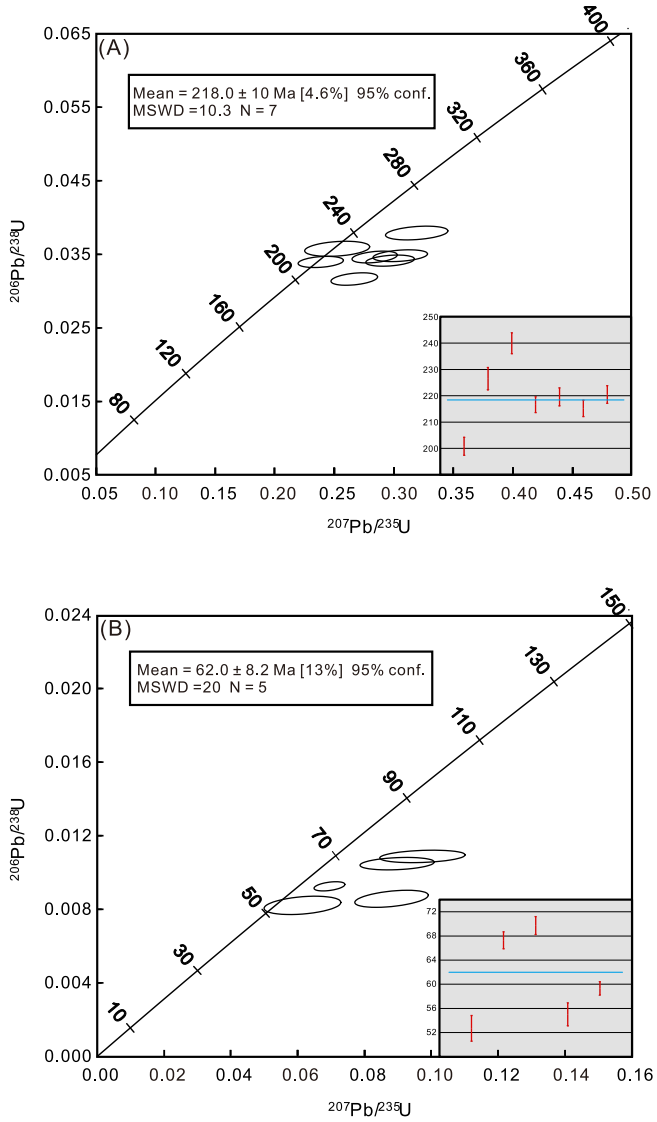

Fig. 11. The U–Pb isochron ages of zircons separated from Mn–Fe carbonate in Zhaxikang deposit: (A) 218 ± 10 Ma; (B) 62 ± 8.2 Ma.

Au, Ag, Mn, Fe, Ba, Ga, In, Tl, B) in the Late Triassic-Early Cretaceous flysch formations formed by turbidity sediment and carbonaceous-siliceous-argillaceous rock series related to hydrothermal sedimentation, and the seafloor hydrothermal system circularly leached these metallogenic elements to form the Pb–Zn minerals in Zhaxikang deposit. (2) the second pulse of mineralization (stages 3 and 4): during syn-collision period (60–42 Ma) of India-Eurasia Plate, influenced by orogeny, the deep source mantle fluid formed by mantle exhaust and the CO_2-bearing fluid formed by Lower crustal dehydration mixed and raised along the shear zone, with the contribution for ore-forming elements from magmatism, to form a series of regional orogenic Au–Sb deposits. This mineralization event is related to the second pulse of mineralization and overprint the first pulse of mineralization in Zhaxikang deposit. (3) the third pulse of mineralization (stages 5 and 6): during post-collision period (25 Ma to now), with the development of STDS, metamorphic core complex and the extensive emplacement of leucogranite, a series of W–Sn, Pb–Zn(Ag) and Sb–Au deposits developed in region. This magmatic-hydrothermal mineralization event is associated with the third pulse of mineralization and also overprints the first and second pulses of mineralization in Zhaxikang deposit.

The marine origin for the first pulse of mineralization and overprint by later two pulses of mineralization have also proved by Fe–Zn isotopic characteristics and fractionation models (Wang et al., 2017, 2018a). Meanwhile, the Keyue Sb–Pb–Zn–Ag deposit, located near Zhaxikang deposit (Fig. 1B), have been linked to these three regional mineralization events by evidence from geology, mineralogy, fluid inclusion, and H–O–S–Pb isotopes, too (Wang et al., 2018b). Nevertheless, although the ores in Pb–Zn mineralization still remain synsedimentary features, the orebodies in Zhaxikang and Keyue deposits are controlled by faults, which not present typical pattern of SEDEX deposits that the bedded orebody occurs in the upper part and the veined orebody occurs in the lower part. Three possible reasons can explain this phenomenon: (1) Due to low exploration level, the bedded orebody have still not been found yet. (2) The location of ore-bearing faults are ancient hydrothermal vents, and due to the collision of India and Eurasia Plates, the Plateau Uplift make the bedded orebody be eroded, and the later tectogenesis form the faults and destroy the orebodies to present form. (3) Large et al. (2005) pointed out the exhalative processes not only can generate bedded orebody in seafloor, but also can develop under seafloor by filling metasomatism, such as the Red Dog SEDEX-type ore district in Alaska (Moore et al., 1987).

6. Conclusions

(1) The Re–Os isotopic system of earlier sulfides from Pb–Zn mineralization should be randomly reset by two later mineralization events with crustal origins.
(2) The precursor zircons in Mn–Fe carbonate are most likely inherited zircons captured from wall rocks, and the younger magmatic zircons should be brought into Mn–Fe carbonate by later hydrothermal fluids from wall rocks and magmatic rocks during recrystallization process.

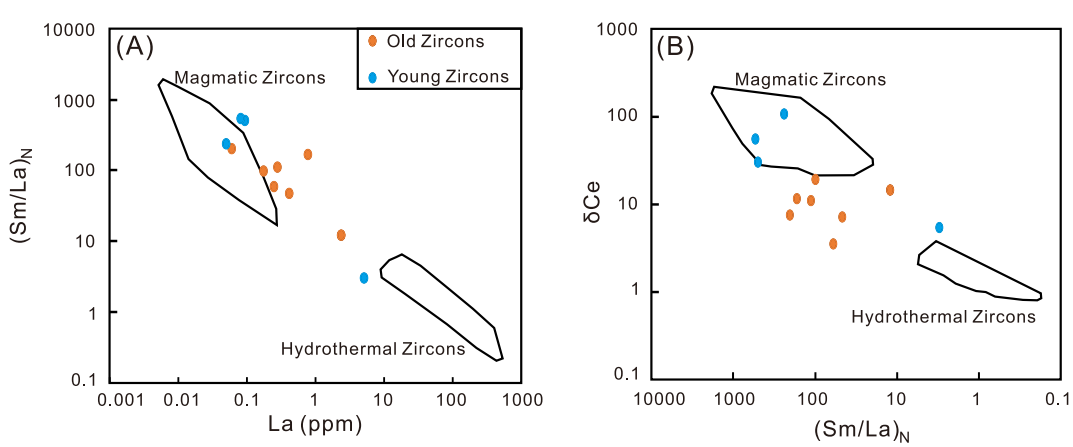

Fig. 12. (A) The "La vs $(Sm/La)_N$" plot for zircons separated from Mn–Fe carbonate in Zhaxikang deposit; (B) The "$(Sm/La)_N$ vs δCe" plot for zircons separated from Mn–Fe carbonate in Zhaxikang deposit (modified from Hoskin, 2005).

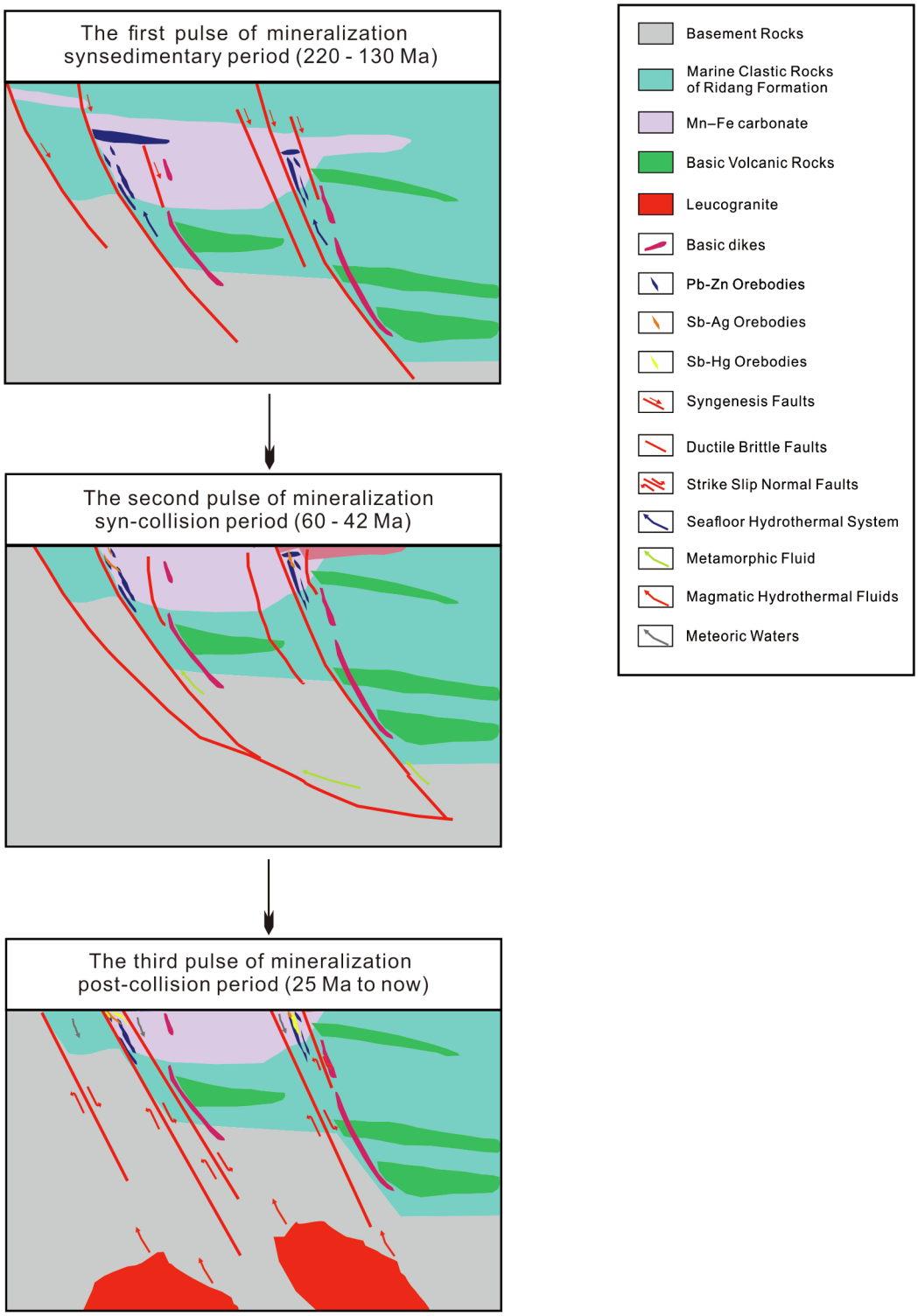

Fig. 13. The ore-forming model for three pulses of mineralization events in Zhaxikang deposit (modified by Wang et al., 2018b).

(3) The Zhaxikang deposit is a superimposed deposit that dominantly experienced three pulses of mineralization corresponding to three regional mineralization events.
(4) The first pulse of mineralization (stages 1 and 2) is related to multiple seafloor volcanic events during synsedimentary period (220–130 Ma) with submarine hydrothermal sedimentation (metasomatism) genesis; the second pulse of mineralization (stages 3 and 4) is associated with the metamorphic fluid system during syn-collision period (60–42 Ma) and overprint earlier Pb–Zn mineralization; and the third pulse of mineralization (stage 5 and 6) relates to the magmatic-hydrothermal activity during post-collision period (25 Ma to now) and also overprints earlier mineralization.

Conflict of interest

We declare that we do not have any commercial or associative interest that represents a conflict of interest in connection with the submitted work.

Acknowledgments

We would like to express our gratitude to Prof. Ali Ucurum and another three anonymous reviewers for their constructive comments and suggestions, which have largely improved this manuscript. This research was supported by the Commonwealth Project from the Ministry of Land and Resources (201511015), Deep Resources Exploration and Mining, National Key R&D Program of China (2018YFC0604104), and Program for Changjiang Scholars and Innovative University Research Teams (IRT14R54, IRT1083).

References

Bian, Q.T., Ding, L., 2006. Discovery of the Zhegucuo Au (As)-bearing fine granular quartz diorite in the eastern Tethyan Himalayan Belt and its significance. Acta. Petrol. Sin. 22, 977–988 (In Chinese with English abstract).
Chen, Y.J., 2006. Orogenic-type deposits and their metallogenic model and exploration potential. Geol. China 33, 1181–1196.
Christensen, J.N., Halliday, A.N., Leigh, K.E., Randell, R.N., Kesler, S.E., 1995. Direct dating of sulfides by Rb–Sr: a critical test using the Polaris Mississippi Valley-type Zn–Pb deposit. Geochim. Cosmochim. Acta 59, 5191–5197.
Coleman, M., Hodges, K., 1995. Evidence for Tibetan plateau uplift before 14 Myr ago from a new minimum age for east-west extension. Nature 374, 49.
Creaser, R.A., Papanastassiou, D.A., Wasserburg, G.J., 1991. Negative thermal ion mass spectrometry of osmium, rhenium and iridium. Geochim. Cosmochim. Acta 55, 397–401.
Duan, J.L., Tang, J.X., Lin, B., 2016. Zinc and lead isotope signatures of the Zhaxikang Pb Zn deposit, South Tibet: implications for the source of the ore-forming metals. Ore Geol. Rev. 78, 58–68.
Frei, R., Nägler, T.F., Schönberg, R., Kramers, J.D., 1998. Re-Os, Sm-Nd, U-Pb, and stepwise lead leaching isotope systematics in shear-zone hosted gold mineralization: genetic tracing and age constraints of crustal hydrothermal activity. Geochim. Cosmochim. Acta 62, 1925–1936.
Geng, J.Z., Qiu, K.F., Gou, Z.Y., Yu, H.C., 2017. Tectonic regime switchover of Triassic Western Qinling Orogen: constraints from LA-ICP-MS zircon U-Pb geochronology and Lu–Hf isotope of Dangchuan intrusive complex in Gansu, China. Chemie der Erde/Geochemistry 77 (4), 673–1651.
Harrison, T.M., Copeland, P., Kidd, W.S.F., Yin, A., 1992. Raising Tibet. Science 255, 1663–1670.
Harrison, T.M., Copeland, P., Kidd, W.S.F., Lovera, O.M., 1995. Activation of the Nyainqentanghla shear zone: implications for uplift of the southern Tibetan plateau. Tectonics 14, 658–676.
Hoskin, P.W.O., Schaltegger, U., 2003. The composition of zircon and igneous and metamorphic petrogenesis. Rev. Mineral. Geochem. 53, 27–62.
Hoskin, P.W.O., 2005. Trace-element composition of hydrothermal zircon and the alteration of hadean zircon from the jack hills, Australia. Geochim. Cosmochim. Acta 69, 637–648.
Hou, Z.Q., Tian, S.H., Yuan, Z.X., Xie, Y.L., Yin, S.P., Yi, L.S., Fei, H.K., Yang, Z.M., 2006. The Himalayan collision zone carbonatites in western Sichuan, SW China: petrogenesis, mantle source and tectonic implication. Earth Planet. Sci. Lett. 244, 234–250.
Jeffrey, L., Hacker, B.R., Dinklage, W.S., Yu, W., Phillip, G., Andrew, C., Wang, J.L., Chen, W.J., Ann, E.B., William, M., 2000. Evolution of the Kangmar dome, southern Tibet: structural, petrologic, and thermochronologic constraints. Tectonics 19, 872–895.
Jiang, S.H., Nie, F.J., Hu, P., Liu, Y., Lai, X.R., 2007. Geochemical characteristics of the mafic dyke swarms in South Tibet. Acta Geol. Sin. 81, 60–71 (In Chinese with English abstract).
Kapp, P., Taylor, M., Stockli, D., Ding, L., 2008. Development of active low-angle normal fault systems during orogenic collapse: insight from Tibet. Geology 36, 7–10.
Large, R.R., Bull, S.W., Mcgoldrick, P.J., Walters, S.G., 2005. Stratiform and strata-bound Zn-Pb-Ag deposits in Proterozoic sedimentary basins, northern Australia. In: Salt Lake City Annual Meeting. pp. 931–963.
Leach, D.L., Bradley, D.C., Huston, D., Pisarevsky, S.A., Taylor, R.D., Gardoll, S.J., 2010. Sediment-hosted lead-zinc deposits in earth history. Econ. Geol. 105, 593–625.
Li, C.F., Li, X.H., Guo, J.H., Li, X.H., Li, H.K., Zhou, H.Y., Li, G.Z., 2011. Single-step separation of Rb-Sr and Pb from minor rock samples and high precision determination using thermal ionization mass spectrometry. Geochimica 40, 399–406 (In Chinese with English abstract).
Li, G.M., Zhang, L.K., Jiao, Y.J., Xia, X.B., Dong, S.L., Fu, J.G., Liang, W., Zhang, Z., Wu, J.Y., Dong, L., Huang, Y., 2017. First discovery and implications of Cuonadong superlarge Be-W-Sn polymetallic deposit in Himalayan metallogenic belt, southern Tibet. Mineral Deposits 36, 1003–1008 (In Chinese with English abstract).
Liang, W., Hou, Z.Q., Yang, Z.S., Li, Z.Q., Huang, K.X., Zhang, S., Li, W., Zheng, Y.C., 2013. Remobilization and overprinting in the Zhaxikang Pb-Zn-Ag-Sb polymetal ore deposit, Southern Tibet: implications for its metallogenesis. Acta. Petrol. Sin. 29, 3828–3842 (In Chinese with English abstract).
Lin, B., Tang, J.X., Zheng, W.B., Leng, Q.F., Yang, C., Tang, X.Q., Hang, Y., Wang, Y.Y., Tan, J.Y., 2014. Petrochemical features, zircon U-Pb dating and Hf isotopic composition of the rhyolite in Zhaxikang deposit, Southern Xizang (Tibet). Geol. Rev. 60, 178–189 (In Chinese with English abstract).
Liu, Y., Gao, S., Hu, Z., Gao, C., Zong, K., Wang, D., 2010. Continental and oceanic crust recycling-induced melt–peridotite interactions in the Trans-North China Orogen: U-Pb dating, Hf isotopes and trace elements in zircons from mantle xenoliths. J. Petrol. 51, 537–571.
Ludwig, K.R., 2003. User's Manual for Isoplot 3.0: A Geochronological Toolkit for Microsoft Excel. Berkeley Geochronology Center Special, Publication No. 4.
Mathur, R., Ruiz, J., Munizaga, F., 2000. Relationship between copper tonnage of Chilean base-metal porphyry deposits and Os isotope ratios. Geology 28, 555–558.
Mathur, R., Marschik, R., Ruiz, J., Munizaga, F., Leveille, R.A., Martin, W., 2002. Age of mineralization of the Candelaria Fe oxide Cu-Au deposit and the origin of the Chilean iron belt, based on Re-Os isotopes. Econ. Geol. 97, 59–71.
McCandless, T.E., Ruiz, J., Campbell, A.R., 1993. Rhenium behavior in molybdenite in hypogene and near-surface environments: implications for Re-Os geochronometry. Geochim. Cosmochim. Acta 57, 889–905.
Mcdonough, W.F., Sun, S.S., 1995. The composition of the earth. Chem. Geol. 120, 223–253.
Meisel, T., Walker, R.J., Morgan, J.W., 1996. The osmium isotopic composition of the Earth's primitive upper mantle. Nature 383, 517.
Meng, X.J., Yang, Z.S., Qi, X.X., Hou, Z.Q., Li, Z.Q., 2008. Silicon-oxygen-hydrogen isotopic compositions of Zhaxikang antimony polymetallic deposit in Southern Tibet and its responses to the ore-controlling structure. Acta. Petrol. Sin. 24, 1649–1655 (In Chinese with English abstract).
Moore, D.W., Young, L.E., Modene, J.S., Plahuta, J.T., 1987. Geologic setting and genesis of the Red Dog zinc-lead-silver deposit, western Brooks Range, Alaska. Econ. Geol. 81, 1696–1727.
Nakai, S., Masuda, A., Shimizu, H., Lu, Q., 1989. La-Ba dating and Nd and Sr isotope studies on the Baiyun Obo rare earth element ore deposits, Inner Mongolia, China. Econ. Geol. 84, 2296–2299.
Nakai, S.I., Halliday, A.N., Kesler, S.E., Jones, H.D., 1990. Rb–Sr dating of sphalerites from Tennessee and the genesis of Mississippi Valley type ore deposits. Nature 346, 354.
Nakai, S.I., Halliday, A.N., Kesler, S.E., Jones, H.D., Kyle, J.R., Lane, T.E., 1993. Rb-Sr dating of sphalerites from Mississippi Valley-type (MVT) ore deposits. Geochim. Cosmochim. Acta 57, 417–427.
Nie, F.J., Hu, P., Jiang, S.H., Li, Z.Q., Liu, Y., 2005. Type and temporal-spatial distribution of gold and antimony deposits (prospects) in Southern Tibet, China. Acta Geol. Sin. 79, 374–384 (In Chinese with English abstract).
Ostendorf, J., Henjes-Kunst, F., Mondillo, N., Boni, M., Schneider, J., Gutzmer, J., 2015. Formation of Mississippi Valley–type deposits linked to hydrocarbon generation in extensional tectonic settings: evidence from the Jabali Zn-Pb-(Ag) deposit (Yemen). Geology 43, 1055–1058.
Ostendorf, J., Henjes-Kunst, F., Schneider, J., Melcher, F., Gutzmer, J., 2017. Genesis of the carbonate-hosted Tres Marias Zn-Pb-(Ge) deposit, Mexico: constraints from Rb-Sr sphalerite geochronology and Pb isotopes. Econ. Geol. 112, 1075–1087.
Pan, G.T., Mo, X.X., Hou, Z.Q., Zhu, D.C., Wang, L.Q., Li, G.M., Zhao, Z.D., Geng, Q.R., Liao, Z.L., 2006. Spatial-temporal framework of the Gangdese Orogenic Belt and its evolution. Acta Petrol. Sin. 22, 521–533 (In Chinese with English abstract).
Pettke, T., Diamond, L.W., 1996. Rb–Sr dating of sphalerite based on fluid inclusion–host mineral isochrones: a clarification of why it works. Econ. Geol. 91, 951–956.
Qiu, B.B., Zhu, D.C., Zhao, Z.D., Wang, L.Q., 2010. The westward extension of Comei fragmented large igneous province in southern Tibet and its implications. Acta Petrol. Sin. 26, 2207–2216 (In Chinese with English abstract).
Qiu, K.F., Yang, L.Q., 2011. Genetic feature of monazite and its U-Th–Pb dating: critical considerations on the tectonic evolution of Sanjiang Tethys. Acta Petrol. Sin. 27, 2721–2732 (in Chinese with English abstract).
Qiu, K.F., Li, N., Taylor, R.D., Song, Y.H., Song, K.R., Han, W.Z., Zhang, D.X., 2014. Timing and duration of metallogeny of the Wenquan deposit in the West Qinling, and its constraint on a proposed classification for porphyry molybdenum deposits. Acta. Petrol. Sin. 30, 2631–2643 (In Chinese with English abstract).
Qiu, K.F., Deng, J., Taylor, R.D., Song, K.R., Song, Y.H., Li, Q.Z., Goldfarb, R.J., 2016. Paleozoic magmatism and porphyry Cu-mineralization in an evolving tectonic setting in the North Qilian Orogenic Belt, NW China. J. Asian Earth Sci. 122, 20–40.
Qiu, K.F., Deng, J., 2017. Petrogenesis of granitoids in the Dewulu skarn copper deposit: implications for the evolution of the Paleotethys ocean and mineralization in Western Qinlin, China. Ore Geol. Rev. 90, 1078–1098.
Searle, M.P., Parrish, R.R., Hodges, K.V., Hurford, A., Ayres, M.W., Whitehouse, M.J., 1997. Shisha Pangma leucogranite, South Tibetan Himalaya: field relations, geochemistry, age, origin and emplacement. J. Geol. 105, 295–317.
Shirey, S.B., Walker, R.J., 1995. Carius tube digestion for low-blank rhenium-osmium analysis. Anal. Chem. 67, 2136–2141.
Su, W., Hu, R., Xia, B., Xia, Y., Liu, Y., 2009. Calcite Sm-Nd isochron age of the Shuiyindong Carlin-type gold deposit, Guizhou. China. Chem. Geol. 258, 269–274.
Sun, X., Zheng, Y.Y., Pirajno, F., McCuaig, T.C., Yu, M., Xia, S.L., Song, Q.J., Chang, H.F., 2018. Geology, S-Pb isotopes, and 40Ar/39Ar geochronology of the Zhaxikang Sb–Pb–Zn–Ag deposit in Southern Tibet: implications for multiple mineralization events at Zhaxikang. Miner. Deposita 53, 435–458.
Suzuki, K., Kagi, H., Nara, M., Takano, B., Nozaki, Y., 2000. Experimental alteration of molybdenite: evaluation of the Re–Os system, infrared spectroscopic profile and polytype. Geochim. Cosmochim. Acta 64, 223–232.
Tong, J.S., Liu, J., Zhong, H.M., Xia, J., Lu, R.K., Li, Y.H., 2007. Zircon U-Pb dating and geochemistry of mafic dike swarms in the Lhozag area, southern Tibet, China, and their tectonic implications. Geol. Bull. China 26, 1654–1664 (In Chinese with English abstract).
Walker, R.J., Carlson, R.W., Shirey, S.B., Boyd, F.R., 1989. Os, Sr, Nd, and Pb isotope systematics of southern African peridotite xenoliths: implications for the chemical evolution of subcontinental mantle. Geochim. Cosmochim. Acta 53, 1583–1595.
Wang, D., Sun, X., Zheng, Y.Y., Wu, S., Xia, S.L., Chang, H.F., Yu, M., 2017. Two pulses of mineralization and genesis of the Zhaxikang Sb–Pb–Zn–Ag deposit in southern Tibet:

constraints from Fe–Zn isotopes. Ore Geol. Rev. 84, 347–363.
Wang, D., Zheng, Y.Y., Mathur, R., Wu, S., 2018a. The Fe–Zn isotopic characteristics and fractionation models: implications for the genesis of the Zhaxikang Sb–Pb–Zn–Ag deposit in Southern Tibet. Geofluids 2018, 1–23.
Wang, D., Zheng, Y.Y., Yang, W.T., Gyatso, N., 2018b. Geology, mineralogy, fluid inclusion and H-O–S–Pb isotopes constraints on ore genesis of the Keyue Sb–Pb–Zn–Ag deposit in Southern Tibet. Geofluids 2018, 1–32.
Wang, Y.X., Go, L.X., Zhang, Z.Z., Wu, C.Z., Zhang, K.J., Li, H.M., Yang, J.D., 2006. Geochronology and Nd-Sr-Pb isotops of the bimodal volcanic rocks of the Bogda rift. Acta. Petrol. Sin. 22, 1215–1224 (In Chinese with English abstract).
Williams, H., Turner, S., Kelley, S., Harris, N., 2001. Age and composition of dikes in southern Tibet: new constraints on the timing of east-west extension and its relationship to postcollisional volcanism. Geology 29, 339–342.
Wu, M.Q., Tian, B.F., Zhang, D.H., Xu, G.Z., Xu, W.X., Qiu, K.F., 2018. Zircon of the No. 782 deposit from the Great Xing'an Range in NE China: implications for Nb-REE-Zr mineralization during magmatic-hydrothermal evolution. Ore Geol. Rev. 102, 284–299.
Xie, Y.L., Li, L., Wang, B., Li, G.M., Liu, H.F., Li, Y.X., Dong, S.L., Zhou, J.J., 2017. Genesis of the Zhaxikang epithermal Pb-Zn-Sb deposit in southern Tibet, China: evidence for a magmatic link. Ore Geol. Rev. 80, 891–909.
Yang, Z.S., Hou, Z.Q., Meng, X.J., Liu, Y.C., Fei, H.C., Tian, S.H., Li, Z.Q., Gao, W., 2009. Post-collisional sb and au mineralization related to the South Tibetan detachment system, Himalayan orogen. Ore Geol. Rev. 36, 194–212.
Yin, A., 2000. Mode of Cenozoic east-west extension in Tibet suggesting common origin of rifts in Asia during the Indo-Asian collision. J. Geophys. Res. 105, 21745–21759.
Yin, A., 2006. Cenozoic tectonic evolution of the Himalayan orogen as constrained by along-strike variation of structural geometry, exhumation history, and foreland sedimentation. Earth Sci. Rev. 76, 1–131.
Yin, A., Harrison, T.M., 2000. Geologic evolution of the Himalayan-Tibetan orogen. Annu. Rev. Earth Planet. Sci. 28, 211–280.
Yu, M., 2015. Characteristics of ore geology and ore-forming fluid in the Zhaxikang Sb-Pb-Zn-Ag deposit, Southern Tibet, China. China University of Geoscience, Beijing Master's Thesis, (In Chinese).
Yin, A., Kapp, P.A., Murphy, M.A., Manning, C.E., Harrison, M.H., Grove, M., Lin, D., Deng, X.G., Wu, C.M., 1999. Significant Late Neogene east-west extension in northern Tibet. Geology 27, 78–790.
Zeng, L.S., Gao, L.E., Dong, C., Tang, S., 2012. High-pressure melting of metapelite and the formation of Ca-rich granitic melts in the Namche Barwa massif, southern Tibet. Gondwana Res. 21, 138–151.
Zhang, J.F., 2010. The Genesis study of Zhaxikang Lead Zinc Antimony Silver Deposit, North Himalayan. China University of Geoscience, Wuhan, pp. 86 Chapter 4, Master's Thesis, (In Chinese).
Zhang, J.F., Zheng, Y.Y., Zhang, G.Y., Gao, S.B., Ye, X.R., Zhang, Z., Liu, M.Y., Li, J.Q., 2010. Genesis of Zhaxikang Pb-Zn-Sb-Ag deposit in northern Himalaya: constraints from multi-isotope geochemistry. Earth Sci. 35, 1000–1010 (In Chinese with English abstract).
Zheng, Y.Y., Liu, M.Y., Sun, X., Yuan, E.H., Tian, L.M., Zheng, H.T., Zhang, G.Y., Zhang, L.H., 2012. Type, discovery process and significance of Zhaxikang antimony polymetallic ore deposit. Tibet. Earth Sci. 37, 1004–1014 (In Chinese with English abstract).
Zheng, Y.Y., Sun, X., Tian, L.M., Zheng, H.T., Miao, Y., Yang, W.T., Zhou, T.C., Geng, X.B., 2014. Mineralization, deposit type and metallogenic age of the gold antimony polymetallic belt in the eastern part of north Himalayan. Geotectonica Et Metallogenia 38, 108–118 (In Chinese with English abstract).
Zhong, H., Xia, J., Tong, J., Lu, R., Li, Y., Xu, S., 2004. New results and major progress in regional geological survey of the Lhozag County Sheet. Regional Geol. China 23, 451–457 (In Chinese with English abstract).
Zhou, Q., Li, W.C., Qing, C.S., Lai, Y., Li, Y.X., Liao, Z.W., Wu, J.Y., Wang, S.W., Dong, L., Tian, E., 2018. Origin and tectonic implications of the Zhaxikang Pb–Zn–Sb–Ag deposit in northern Himalaya: evidence from structures, Re–Os–Pb–S isotopes, and fluid inclusions. Miner. Deposita 53, 585–600.
Zhu, D.C., Chung, S.L., Mo, X.X., Zhao, Z.D., Niu, Y.L., Song, B., Yang, Y.H., 2009. The 132 Ma Comei-Bunbury large igneous province: remnants identified in present-day southeastern Tibet and southwestern Australia. Geology 37, 583–586.